AGU PUBLICATIONS

JGR

Journal of Geophysical Research: Space Physics

RESEARCH ARTICLE
10.1002/2016JA023587

Key Points:
- Martian plasma system response to space weather disturbances during low solar activity
- Propagation of an ICME-like transient and a fast solar wind stream from STEREO-B to Mars
- Longitudinal and radial inner boundary movements at Mars

Correspondence to:
B. Sánchez-Cano,
bscmdr1@leicester.ac.uk

Citation:
Sánchez-Cano, B., et al. (2017), Mars plasma system response to solar wind disturbances during solar minimum, *J. Geophys. Res. Space Physics*, *122*, 6611–6634, doi:10.1002/2016JA023587.

Received 14 OCT 2016
Accepted 18 MAY 2017
Accepted article online 22 MAY 2017
Published online 7 JUN 2017

Mars plasma system response to solar wind disturbances during solar minimum

B. Sánchez-Cano[1], B. E. S. Hall[1], M. Lester[1], M. L. Mays[2], O. Witasse[3], R. Ambrosi[4], D. Andrews[5], M. Cartacci[6], A. Cicchetti[6], M. Holmström[7], S. Imber[1], P. Kajdič[8], S. E. Milan[1], R. Noschese[6], D. Odstrcil[9], H. Opgenoorth[5], J. Plaut[10], R. Ramstad[7], and K. I. Reyes-Ayala[8]

[1]Radio and Space Plasma Physics Group, Department of Physics and Astronomy, University of Leicester, Leicester, UK, [2]Heliophysics Science Division, NASA Goddard Space Flight Center, Greenbelt, Maryland, USA, [3]European Space Agency, ESTEC-Scientific Support Office, Noordwijk, Netherlands, [4]Space Research Centre, Department of Physics and Astronomy, University of Leicester, Leicester, UK, [5]Swedish Institute of Space Physics, Uppsala, Sweden, [6]Istituto di Astrofisica e Planetologia Spaziali, Istituto Nazionale di Astrofisica, Rome, Italy, [7]Swedish Institute of Space Physics, Kiruna, Sweden, [8]Instituto de Geofísica, Universidad Nacional Autónoma de México, Ciudad Universitaria, Mexico City, Mexico, [9]School of Physics, Astronomy, and Computational Sciences, George Mason University, Fairfax, Virginia, USA, [10]Jet Propulsion Laboratory, Pasadena, California, USA

Abstract This paper is a phenomenological description of the ionospheric plasma and induced magnetospheric boundary (IMB) response to two different types of upstream solar wind events impacting Mars in March 2008, at the solar minimum. A total of 16 Mars Express orbits corresponding to five consecutive days is evaluated. Solar TErrestrial RElations Observatory-B (STEREO-B) at 1 AU and Mars Express and Mars Odyssey at 1.644 AU detected the arrival of a small transient interplanetary coronal mass ejection (ICME-like) on the 6 and 7 of March, respectively. This is the first time that this kind of small solar structure is reported at Mars's distance. In both cases, it was followed by a large increase in solar wind velocity that lasted for ~10 days. This scenario is simulated with the Wang-Sheeley-Arge (WSA) - ENLIL + Cone solar solar wind model. At Mars, the ICME-like event caused a strong compression of the magnetosheath and ionosphere, and the recovery lasted for ~3 orbits (~20 h). After that, the fast stream affected the upper ionosphere and the IMB, which radial and tangential motions in regions close to the subsolar point are analyzed. Moreover, a compression in the Martian plasma system is also observed, although weaker than after the ICME-like impact, and several magnetosheath plasma blobs in the upper ionosphere are detected by Mars Express. We conclude that, during solar minimum and at aphelion, small solar wind structures can create larger perturbations than previously expected in the Martian system.

1. Background

Planetary space weather events often produce large variations in the particle and electromagnetic radiation incident upon a planet. At Earth, where the atmosphere and ionosphere are protected by a global magnetosphere of internal origin, such variations can lead to disturbances of the "quiet time" magnetosphere and ionosphere, commonly referred to as geomagnetic storms [e.g., *Schunk and Nagy*, 2009, and reference therein] or ionospheric storms [e.g., *Prolss*, 1995; *Buonsanto*, 1999]. At Mars, where the atmosphere and ionosphere are not protected by any global-scale intrinsic magnetic field [*Acuña et al.*, 1999] and are directly exposed to the incoming solar wind, the response of the plasma system to each of these events is often unusual and with differing characteristics [see, e.g., *Opgenoorth et al.*, 2013].

Stream interaction regions (SIRs) are structures formed by the interaction between slow and fast solar wind streams that create a region of compressed and heated plasma at the leading edge of the high-speed stream [e.g., *Richardson et al.*, 1996; *Gosling and Pizzo*, 1999]. These structures are characterized by enhanced density and magnetic field strength in the solar wind near the ecliptic plane [e.g., *Alves et al.*, 2006]. Their primary origin is the solar coronal holes that produce fast solar wind streams, and they constitute the most important source of geomagnetic disturbances at Earth, especially during the declining and minimum phases of a solar cycle [e.g., *Grandin et al.*, 2015, and references therein].

Coronal mass ejections (CMEs) are explosions of magnetic field and plasma from the Sun's corona and are often accompanied by large solar flares. When CMEs reach interplanetary space, they are called interplanetary coronal mass ejections (ICMEs). CMEs originate from highly twisted magnetic field structures, or "flux

ropes", on the Sun, which are normally associated with relatively cold plasma trapped on the flux ropes within the Sun's corona. Since CMEs have an embedded magnetic field that is stronger than the background field of the solar wind, they expand in size as they propagate outward from the Sun. In comparison to SIRs, they are radial solar transients, passing through the solar system with speeds of up to 2500 km s^{-1}. They consist of different regions observed in the solar wind, such as a shock, plasma sheath, solar wind pileup, ejecta, compression regions, and driver gas [*Rouillard*, 2011], although in the slowest ones, the shock and sheath are often not observed. The full transit of the ejecta of an ICME across an inner solar system body can last 1–2 days, often causing stronger impacts on planetary plasma environments than SIRs [*Prise et al*., 2015]. ICMEs are most likely to occur during moderate to high solar activity periods, since they are related to the Sun's activity cycle, although they can also occur during low activity phases of the solar cycle, albeit being generally smaller than at other phases of the solar cycle.

Small transient ICME-like structures have been found to be associated with magnetic field rotations lasting less than half a day, reduced magnetic field fluctuations and an associated drop in plasma β (ratio of plasma and magnetic field pressures) [*Rouillard et al*., 2011]. These small solar wind structures often produce sharp and large changes in the solar wind dynamic pressure and frequently have some classical ICME signatures but with weaker magnetic fields ($<$ 7 nT) and/or short durations ($<$ 10 h) [e.g., *Rouillard et al*., 2011; *Kilpua et al*., 2012; *Jian et al*., 2013; *Xie et al*., 2015]. These events do not drive interplanetary shocks, nor do they exhibit significant gradients across the structure (they are not expanding structures), but instead appear to move with the surrounding flow and may be considered as simply floating within the solar wind [*Kilpua et al*., 2009]. Moreover, ICME-like transients are commonly registered very close to SIR regions and in declining parts of fast solar wind streams, suggesting that they tend to arise close to coronal hole boundaries, most probably having an important role in coronal hole dynamics [*Kilpua et al*., 2012].

Our knowledge of the Martian ionospheric response to these kinds of events comes from several pieces of work carried out during the last few years, most of them during the moderate-ascending and high activity phases of the solar cycle, when the ionosphere is more robust and the obstacle created by the Martian plasma system is strong enough to compete with the solar wind [e.g., *Sánchez-Cano et al*., 2016]. In a global view, the associated shock of a powerful ICME often produces an enhancement of energetic electrons and an increase in the solar energetic particles (SEPs) [e.g., *Morgan et al*., 2014; *Prise et al*., 2015; *Jakosky et al*., 2015] that may produce aurora [e.g., *Jakosky et al*., 2015]. The sharp increase in solar wind dynamic pressure causes a strong compression of the full Martian plasma system, which is manifested as an obvious reduction in boundary locations [e.g., *Dong et al*., 2015]. The ionosphere is also strongly compressed [e.g., *Morgan et al*., 2014], with a more intense presence of induced magnetic field at ionospheric altitudes [e.g., *Opgenoorth et al*., 2013]. Moreover, there is an extension of the cold plasma population deeper into the nightside which exhibits wavelike and turbulent motion [*Morgan et al*., 2014], and flux ropes can be visible in the nightside flank magnetosheath at high altitudes, $>$5000 km, with intensities of ~80 nT [*Hara et al*., 2016]. On the other hand, during moderate and high solar cycle phases, the effects of a SIR on the Martian plasma environment can seem similar to those caused by an ICME [*Opgenoorth et al*., 2013], although the main difference is the longer duration of the plasma variations within an ICME-related event. This is most probably related to the longer duration of the ICME ejecta passing by the planet [*Opgenoorth et al*., 2013]. For these solar activity conditions, *Opgenoorth et al*. [2013] revealed that the combination of simultaneously increased velocity and increased solar wind density was a more efficient driver for magnetospheric/ionospheric responses at Mars than velocity or density by itself. In this line, simulations indicate that ionospheric perturbations in density, magnetic field, and velocity can last for a few hours after the solar wind returns to the quasi-equilibrium state [*Ma et al*., 2014].

There are other solar wind disturbances that can also have a major role in the behavior of the Martian plasma system, such as solar flares. For example, *Futaana et al*. [2008] studied the effect of a geoeffective solar flare in December 2006 (close to the solar minimum phase) with multipoint observations made by Venus Express, Mars Express, and Earth-based satellites. The SEPs associated with that flare created a sporadic enhancement of about 1 order of magnitude in the heavy ion escaping flux at Mars, which makes evident the high potential that space weather has on the process of planetary atmospheric evolution. Moreover, *Lillis et al*. [2012] showed that peak SEP ionization rates on the nightside during a large solar storm in 2003 (moderate to high solar activity) were comparable to typical dayside photoionization rates and at least 3 orders of magnitude higher than average nightside electron impact ionization rates.

At solar minimum, the obstacle created by the Martian plasma system is weaker since the ionosphere is much thinner. Recently, *Sánchez-Cano et al*. [2016] demonstrated the behavior of the ionospheric total electron content (TEC) with the solar cycle (from mid-2005 to mid-2012), which indicated a major TEC reduction directly related to the large decrease in the solar EUV and X-ray fluxes observed during the low solar activity period of solar cycle 23/24. During this time, especially in 2008, the maximum thermal ionospheric pressure was at its lowest levels (more than a factor 2 smaller than at the high solar activity phase). Therefore, during the solar minimum, the ionospheric response to short-term variations of the solar wind might be expected to be different from that at high solar activity levels. However, this scenario is poorly understood. *Dubinin et al*. [2009] showed for the first time that SIRs at solar minimum cause strong perturbations in the Martian-induced magnetosphere and ionosphere. The Martian magnetic barrier formed by the pileup of the draped interplanetary magnetic field, the magnetic pileup boundary (MPB), and the induced magnetospheric boundary (IMB) cease to be a shield for the incoming solar wind, and large "blobs" of solar wind plasma penetrate into the induced magnetosphere, capturing and sweeping out dense plasma from the ionosphere. As a consequence, the topside Martian ionosphere (~300 km) becomes very fragmented consisting of intermittent cold/low energy and energized plasmas. On the other hand, *Ramstad et al*. [2015] showed that for low solar wind densities and low EUV intensities (such as solar minimum), changes in the solar wind velocity play notable effects in modifying plasma dynamics.

As mentioned before, the major part of all of these studies at Mars come from moderate and high solar activity phases of the solar cycle. There are still many open questions about the system response to short-term solar events, which should be answered with simultaneous multispacecraft observations. For example, the solar wind and ionosphere behavior in both the dayside and nightside of Mars has never been covered at the same time for the same space weather event. All the information that we know on this topic comes from MHD simulations. Another important open question is the behavior of the Mars plasma system (from the boundary location to the lower ionosphere of Mars) during the very low solar activity phase when a short time event hits the system. Although a similar behavior might be expected to other phases of the solar cycle, the ionospheric obstacle is very different during this time, as the phase of the solar cycle is a major driver for the general ionosphere state [e.g., *Sánchez-Cano et al*., 2015b, 2016]. This paper tries to answer this question. The paper is focused on the analysis and description of the Martian plasma system's reaction to different transitory space weather events that consecutively hit Mars in March 2008, specifically a small transient ICME-like event, followed by a SIR and a subsequent fast solar wind stream which lasted several days. These events occurred during the comparatively very low solar minimum of solar cycle 23/24 and when Mars was at aphelion. Therefore, they occurred when the Martian ionospheric thermal pressure was at its lowest during the solar cycle. An analysis of the Martian plasma system behavior in response to these events is completed by using several instruments onboard Mars Express (MEX) and Mars Odyssey, as well as a solar wind simulation of this scenario. Finally, a short comparison with other previous studies on this topic, but in other phases of the solar cycle, is given.

The objective of this work is to improve the knowledge of the reaction of the ionosphere and magnetosheath boundaries of Mars during the very low solar activity phase in comparison to all the known reactions during other phases of the solar cycle. Moreover, the propagation and characteristics of an ICME-like structure at Mars's distance are assessed for the first time. This paper frames two different disciplines: heliophysics and planetary space weather.

2. Instrumentation and Solar Wind Model Description

The propagation of the solar events discussed in this paper from the Sun to Mars has been analyzed by using data from the Solar TErrestrial RElations Observatory is the acronym of STEREO satellite, in conjunction with a modeling simulation using the global 3-D MHD ENLIL Model. Once at Mars, the Mars plasma response to such events has been evaluated with different MEX and Mars Odyssey data sets. In this section, we briefly summarize the main characteristics of the instrumentation and modeling used in this work.

Solar wind data, i.e., solar wind velocity, density, and the interplanetary magnetic field come from STEREO-B [*Kaiser et al*., 2008], which is one of the two solar observatory satellites launched in 2006 and placed into orbit around the Sun at 1 AU.

Simulations of the solar wind propagation have been made with the Wang-Sheeley-Arge (WSA)-ENLIL + Cone model available from the Community Coordinated Modeling Center (CCMC). The global 3-D MHD ENLIL model provides a time-dependent description of the background solar wind plasma and magnetic field using the WSA coronal model [*Arge and Pizzo*, 2000; *Arge et al*., 2004] as input at an inner boundary of 21.5 solar radii ($R_\odot$) [*Odstrcil et al*., 1996, 2004; *Odstrcil*, 2003; *Odstrcil and Pizzo*, 1999a, 1999b]. A series of synoptic solar magnetic field maps derived from magnetograms are used as input to WSA-ENLIL as a basis for a time-dependent background solar wind simulation. ENLIL version 2.8f was used in this work, with a time-dependent inner boundary constructed from a series of daily input WSA synoptic maps each computed from a new Global Oscillation Network Group (GONG) [*Harvey et al*., 1996] daily synoptic "QuickReduce" magnetogram every 24 h at the ENLIL inner boundary. Generally, a CME disturbance is inserted in the WSA-ENLIL model as slices of a homogeneous spherical plasma cloud with uniform velocity, density, and temperature as a time-dependent inner boundary condition at 21.5 $R_\odot$ with a constant background magnetic field. Cloud parameters of location, speed, and size can be determined using any technique for deriving CME kinematic properties from coronagraph data. In this study, a low-resolution (4°) simulation was performed on a spherical grid size of $384 \times 30 \times 90$ (r, θ, ϕ), with a range of 0.1 to 2.1 AU in radius (r), −60° to +60° in latitude (θ), and 0° to 360° in longitude (ϕ), Heliocentric Earth Equatorial (HEEQ). The full simulation is available at http://ccmc.gsfc.nasa.gov/database_SH/Beatriz_Sanchez-Cano_033016_SH_1.php.

At Mars, the hot plasma population at the spacecraft altitude, i.e., high energetic electron and ion plasma, is sampled with the Analyzer of Space Plasmas and Energetic Neutral Atoms (ASPERA-3) instrument [*Barabash et al*., 2004], onboard MEX [*Chicarro et al*., 2004]. The ELectron Spectrometer (ELS) experiment is capable of sampling electrons within the energy range of 0.001–20 keV, although electrons at energies <20 eV are typically modulated by the spacecraft potential. The detector has an energy resolution of 8% and an intrinsic field of view (FOV) of 4° (polar) × 360° (azimuth). ELS was designed to have many operational modes (e.g., see, *Frahm et al*. [2006] and *Hall et al*. [2016a] for details of the main modes) but has typically been operated in survey mode which samples electrons across the full energy range in 128 log-spaced steps, completing a full scan in 4 s. The design specification of the ion mass analyzer (IMA) was to sample ions across the energy range of 10 eV/q–30 keV/q [*Yamauchi et al*., 2015; *Hall et al*., 2016b] and to be able to mass resolve the main ion species within the Martian plasma environment (masses of 1, 2, 4, 16, and 32 amu/q). IMA has an energy resolution of 7% and a FOV of 90° (polar) × 360° (azimuth). Sampling across the polar FOV is broken into 16 elevation steps (−45° to 45°), with a single step taking 12 s, and a full FOV scan taking 192 s.

The Martian cold plasma population (energies <1 eV) is analyzed with The Mars Advanced Radar for Subsurface and Ionospheric Sounding (MARSIS) [*Picardi et al*., 2004] onboard MEX. This instrument has been probing the ionosphere and subsurface of Mars since mid-June 2005 [*Orosei et al*., 2014]. A typical MARSIS ionospheric sounding pass can only be done for altitudes less than 1200 km, which means only about 20 min either side of the periapsis [*Gurnett et al*., 2005]. MARSIS has two different operational modes, the active ionospheric sounding (AIS) mode and the subsurface mode, from which multiple ionospheric parameters can be obtained. In the AIS mode [*Gurnett et al*., 2005], MARSIS works as a topside ionospheric sounder, where the ionization from the spacecraft to the maximum ionization region (~135 km for pure dayside conditions) is sampled. The basic data products of this process are the ionograms, graphics of the time delay between the signal being emitted and returned to the radar antennas (after reflection by the ionosphere) versus the transmitted frequency [*Gurnett et al*., 2005]. The vertical electron density profiles of the topside ionosphere (from ~135 km to the spacecraft location) can be obtained by inversion of the main reflection trace in the ionograms [*Sánchez-Cano et al*., 2012; *Morgan et al*., 2013]. In the ionograms closer to periapsis, it is common to also record the local plasma harmonics (local plasma frequency) at the location of the spacecraft altitude [*Andrews et al*., 2013], which is itself another data set and allows for the correct inversion of the topside electron density profiles. Moreover, when the spacecraft is traveling through a region in the presence of a magnetic field at the spacecraft location (either from crustal or solar wind origin), the electron cyclotron frequency is also often recorded in the ionograms. Consequently, the magnitude of the magnetic field at the antenna's location is easily derived [*Gurnett et al*., 2008; *Akalin et al*., 2010; *Andrews et al*., 2015]. In the subsurface mode [*Gurnett et al*., 2005; *Orosei et al*., 2014], MARSIS works as a geophysical radar to analyze the subsurface of the planet. Since the radar signals cross the full atmosphere twice (from MEX to the surface and then back to MEX), the total electron content (TEC) of the entire atmosphere (from Mars surface to spacecraft position) can be retrieved as a by-product [*Safaeinili et al*., 2007; *Mouginot et al*., 2008; *Cartacci et al*., 2013]. Subsurface data, however, are limited in the full dayside when the MARSIS carrier frequency is close to the

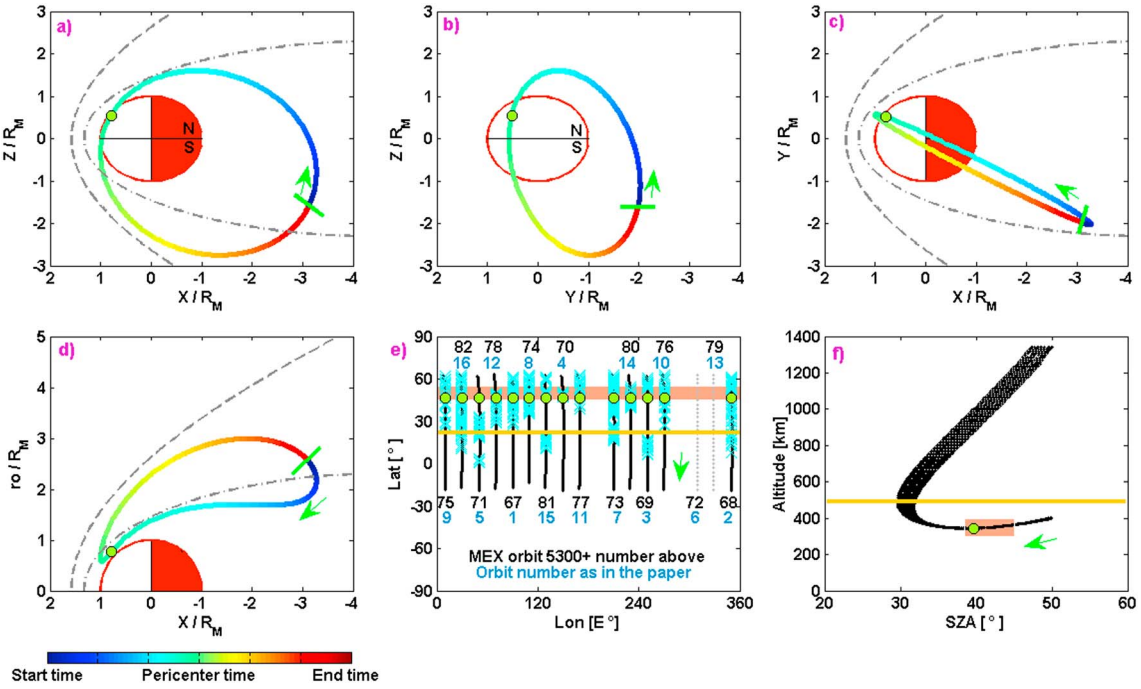

Figure 1. Mars Express orbit configurations from 7 to 11 March 2008. A total of 16 MEX orbits is used in this study. In all the panels, a green dot symbolizes the position of the periapsis and a green arrow the direction of the Mars Express transit. Bow shock (grey dashed line) and MPB (grey dash-dotted line) are from the *Edberg et al.* [2008] model. Orbits in (a–c) three orthogonal planes in Mars solar orbital (MSO) coordinates and in (d) a cylindrically symmetric coordinate system. The small green line indicates the beginning-end of the orbit. (e) Orbital position projected over the planet when its altitude was lower than 1350 km (in black when MARSIS-AIS was in operation and in grey for the rest). To help with the identification, each orbit has been numbered from 1 to 16. For these transits, the position when local plasma at the spacecraft position was higher than 10^8 m^{-3} (clear identification of the ionosphere) has been marked with cyan crosses. Salmon bar indicates the area that data in Figure 7 come from. Yellow line indicates an altitude of 500 km; from top to the yellow line, the altitude is almost constant (see also Figure 1f). (f) Orbits in altitude versus solar zenith angle configuration when MARSIS-AIS was working. Yellow line and salmon fringe have the same meaning as in Figure 1e.

maximum plasma frequency of the ionosphere, and the signal becomes significantly degraded [*Sánchez–Cano et al.*, 2015a]. In this study, subsurface TEC is analyzed through the *Cartacci et al.* [2013] algorithm, only with data that fit the signal-to-noise ratio (SNR) condition of SNR $>$ 25 dB. This conservative approach guarantees the accuracy of the TEC estimation [*Sánchez-Cano et al.*, 2016].

Figure 1 shows the MEX orbit configuration for the period discussed in this paper, i.e., from 7 to 11 March 2008. Orbits are presented in three orthogonal planes of the Mars solar orbital (MSO) coordinate system (Figures 1a–1c), in an axisymmetric MSO coordinate system (Figure 1d), projected over the planet when the altitude was lower than 1350 km (Figure 1e), and altitude versus solar zenith angle (SZA) (Figure 1f). The green dot indicates the pericenter position of the orbits in each panel, which in this study is always in the Northern Hemisphere at about 50° latitude and 40° SZA. The green arrow indicates the direction of the MEX motion. In Figures 1a, 1c, and 1d, the Sun is to the left ($+X_{MSO}$) and the *Edberg et al.* [2008] model bow shock and MPB positions have been superimposed. In Figures 1e and 1f, a yellow line indicates the position at which MEX was below 500 km, and the salmon bar indicates the latitude and SZA intervals from which data in Figure 7 come. Moreover, light blue crosses in Figure 1e indicate the position when the local plasma density at the spacecraft location was higher than 10^8 m^{-3}, which means that the ionosphere was clearly detected during each orbit transit at this time, as will be explained later. During this period, MEX transited from the nightside upper ionosphere into the dayside upper ionosphere via the Northern Hemisphere and later continued through to the Southern Hemisphere where the model MPB was crossed. MEX then transitioned through the southern part of the magnetosheath region moving from the dayside back into the nightside, to finally return to the deep nightside-induced magnetotail close to the orbit apoapsis. We note that a priori based on the *Edberg et al.* [2008] model predictions, MEX would not normally enter the solar wind during this time. The MEX orbit configuration remained similar across all 16 orbits of this study, only changing in

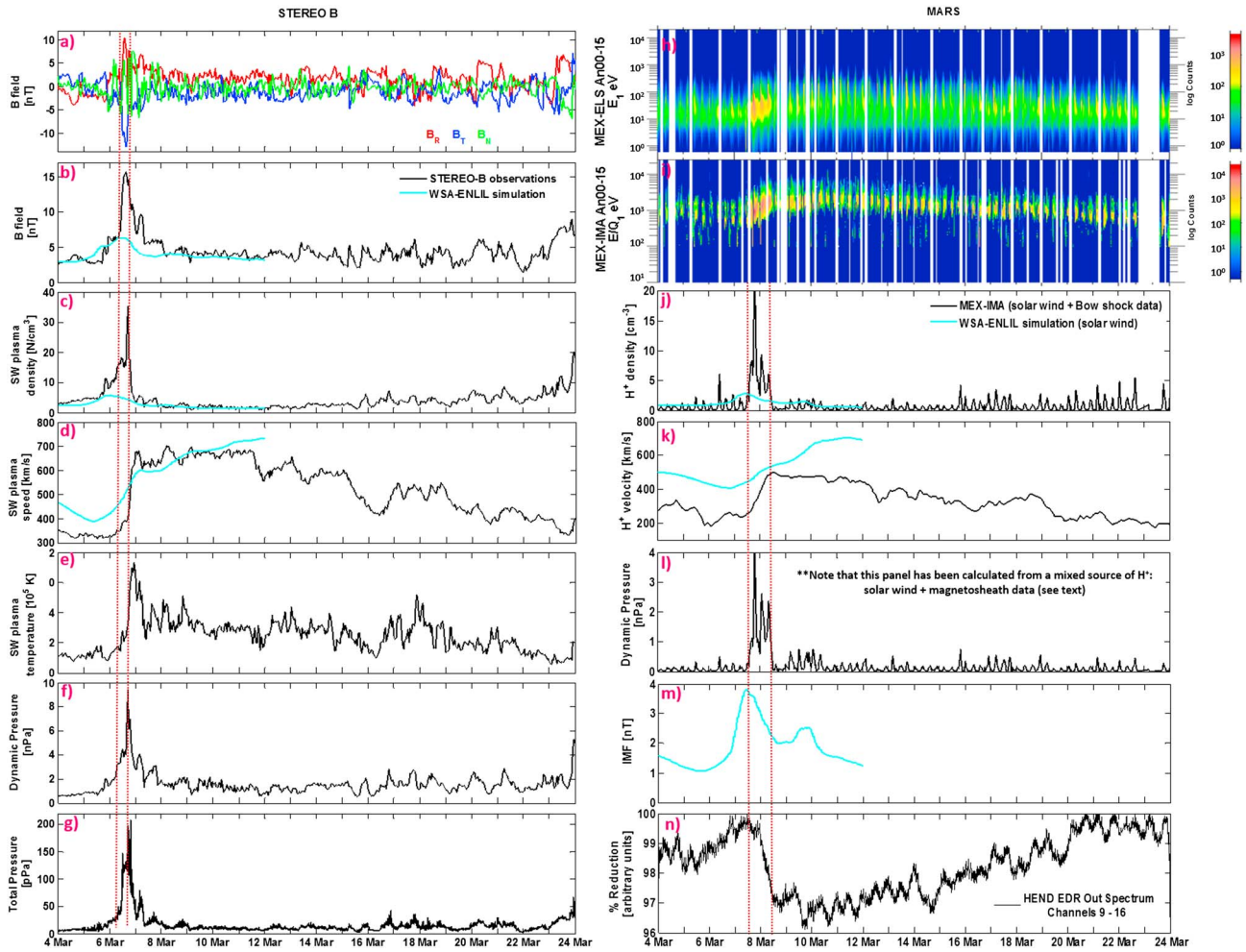

Figure 2. STEREO-B solar wind records: (a) Magnetic field components in Radial Tangential Normal (RTN) coordinates, (b) magnetic field magnitude, (c) solar wind plasma density, (d) velocity, (e) temperature, (f) dynamic pressure, and (g) total pressure (sum of the magnetic pressure and plasma thermal pressure) perpendicular to the magnetic field. Solar wind records at Mars by Mars Express and Mars Odyssey: (h) ASPERA-3 ELS and (i) IMA H^+ spectrograms, (j) ASPERA-3 solar wind (see text) H^+ density and (k) velocity, (l) dynamic pressure (see text for specifications), (m) interplanetary magnetic field only from WSA-ENLIL + Cone model, and (n) percentage of reduction in cosmic rays measured by HEND-Mars Odyssey with respect to the maximum level for this period. In most of the panels, a light blue line shows the WSA-ENLIL + Cone simulation at STEREO-B and Mars. Red vertical dashed lines indicate the ICME-like event passage in each case.

longitude over the planet as illustrated in Figure 1e. This allows us to directly compare data from such orbits without introducing any spatial ambiguity. At suitable MARSIS altitudes (between periapsis and 500 km, Figures 1e and 1f), MEX was located in the Northern Hemisphere and the equatorial region of the Southern Hemisphere, always in the full dayside with SZA between 30 and 50°.

Finally, the effect of the ICME-like structure on the galactic cosmic rays (GCR) that reaches Mars is analyzed with the high-energy neutron detector (HEND) [*Boynton et al.*, 2004] on board the Mars Odyssey spacecraft. The primary mission of this instrument is to collect geochemical data from the surface of Mars, although it also allows the identification of space weather events, [e.g., *Morgan et al.*, 2014]. As explained later (see section 3), the neutron monitoring can be used a proxy of the GCR that reaches Mars, allowing us to identify rapid reductions in the observed GCR intensity after the passage of an ICME (Forbush Decrease). Therefore, it provides confirmation of the ICME arrival. As no mission had a magnetometer at Mars during 2008, it is difficult to discern if the ICME arrived at Mars together with the SIR or if it was only the SIR. However, knowing the behavior of the GCR in relation to certain ICME properties such as the intrinsic magnetic field, this is a powerful data set to identify such events. The HEND instrument is composed of five separate sensors that provide measurements of neutrons in the energy range from 0.4 eV up to 15 MeV [e.g., *Zeitlin et al.*, 2010].

The detector used in this work is the Outer Scintillator (an anticoincidence detector) only in channels 9–16. It provides information on minor to moderate solar particle events. Moreover, in order to compare the percentage level of variation in GCR, data have been normalized with respect to the highest HEND value measured during the time interval of this study.

3. Space Weather Events at 1 and 1.644 AU and Solar Wind Simulation

The detection of any transient space weather event at Mars, such as ICMEs or SIRs, is not always easy due to the lack of a solar wind monitor. During the solar minimum 23/24, there were no spacecraft with a magnetometer at Mars. Moreover, the plasma instruments on MEX were not continuously sampling the solar wind. The Advanced Composition Explorer **(**ACE), Wind, or STEREO-A and STEREO-B placed at 1 AU are commonly used as solar wind monitors for Mars provided there are no significant differences in solar longitude between Earth and Mars [e.g., *Sánchez-Cano et al*., 2015b, 2016]. For this reason, the most possible accurate measurements of the upstream solar wind at Mars occur when Mars and Earth are in apparent opposition. Recently, the Mars Upper Atmosphere Network (MUAN) community [*Opgenoorth et al*., 2010] has been leading coordinated efforts to have several MEX campaigns (with as many plasma instruments operating as possible) when both planets were aligned along the Parker spiral to better understand any plasma variability due to external conditions [*Opgenoorth et al*., 2013]. Also, thanks to this planetary opposition and/or a Mars alignment with any solar wind observatory at 1 AU, a catalogue of 56 possible ICME candidates that could have affected the Mars environment between November 2007 and April 2014 has been recently published. All the events are based on multipoint observations of the propagation of the ICME in the inner solar system. The catalogue is available at [http://usuarios.geofisica.unam.mx/primoz/ICMEs.html].

For this low solar activity study, an event first observed by the STEREO-B satellite at 1 AU on the 6 March 2008 and by MEX and Mars Odyssey at Mars at 1.644 AU on 7 March 2008 has been selected from this catalogue. Figure 2 shows the data recorded by these three missions, as well as a solar wind simulation of the propagation of this event made with the WSA-ENLIL + Cone model (Figures 2 and 3) for a period of 20 days starting on 4 March 2008. STEREO-B and Mars were nearly aligned along the Parker spiral as shown in Figure 3, where their respective positions in the inner solar system are represented.

Figures 2a–2g show the STEREO-B solar wind data to illustrate the ICME-like event. A parent CME at the Sun in the SOHO and STEREO coronagraph data could not be determined. This event was previously analyzed by *Rouillard et al*. [2011] at 1 AU and afterward catalogued by *Kilpua et al*. [2012] as an ICME-like transient event of Category 2 (i.e., followed by a SIR). As seen in Figures 2a–2g, the ICME-like transient was very short in duration (about only 5 h) as detected by STEREO-B on 6 March 2008 between 12:15 UT and 17:00 UT (red vertical lines), and it was immediately followed by a large and abrupt increase of the solar wind speed from about 400 km/s to 700 km/s. This fast solar wind lasted for at least 5 days, as also seen in the high plasma temperature. The interaction region between the ICME-like event and the fast stream region produced an elevated magnetic field magnitude (~15 nT) and a solar wind density peak at the trailing edge of the ICME-like transient. Also, the total perpendicular pressure (sum of the magnetic pressure and plasma thermal pressure perpendicular to the magnetic field), the dynamic pressure, and the plasma temperature increased [*Kilpua et al*., 2012]. As *Rouillard et al*. [2011] stated, the ICME-like structure had a remarkably small extent ($<$0.05 AU), a marked sharp decrease in plasma β (from ~3 to ~0.9), and the magnetic flux rope size was nearly an order of magnitude smaller than those associated with traditional ICMEs.

Figures 2h–2n show the observations made at Mars by ASPERA-3 (MEX) and HEND (Mars Odyssey) instruments for the same interval as Figures 2a–2g. A priori, it is difficult to discern without a proper magnetometer if the ICME-like transient arrived at Mars just before the SIR (as observed at STEREO-B) or if both structures merged during their transit between STEREO-B and Mars. As mentioned in the first section, some studies point out that such ICME-like structures seem to move by "floating" with the surrounding solar wind at least until 1 AU [e.g., *Kilpua et al*., 2009], so it could be the case that this behavior was maintained at least until 1.65 AU.

MEX recorded the arrival of the space weather event in the evening of 7 March 2008, ~29 h later than at STEREO-B (Figures 2h–2l). It caused a significant enhancement in energy in both ELS and IMA H^+ energy spectra (Figures 2h and 2i, respectively) of about 1.5 order of magnitude, respectively, and the associated effects

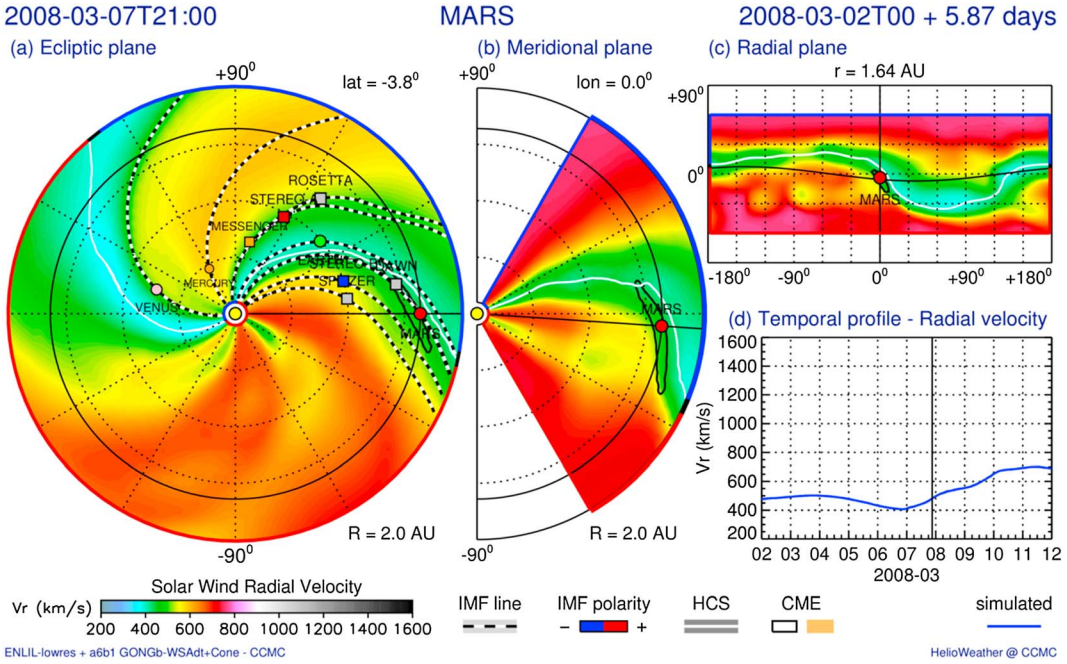

Figure 3. WSA-ENLIL + Cone simulation of the ICME-like, SIR, and fast stream of this study. The simulation is a radial velocity contour plot on 7 March 2008 at 21:00 UT for the (a) ecliptic plane, (b) meridional plane of Mars, and (c) radial plane at 1.64 AU sphere in cylindrical projection, including a hypothetical CME. (d) The simulated radial velocity profile at Mars. Mars appears represented by a red circle, STEREO-B by a blue square, and the Sun by a yellow circle. The black oblong shape that passes through Mars is the simulated ICME. Simulation and animations are available online at http://ccmc.gsfc.nasa.gov/database_SH/Beatriz_Sanchez-Cano_033016_SH_1.php.

lasted for about 1 day. A long fast stream then followed keeping the general enhancement of the electron and ion spectra during several days. As described in the previous section, MEX was not expected to enter the solar wind during this time. However, we note that during that period most probably the MPB/IMB and the bow shock were closer to the planet than expected by the average boundary models [e.g., *Vignes et al.*, 2000; *Edberg et al.*, 2008] because of the low solar activity levels of 2008 plus the fact that Mars was close to aphelion [*Hall et al.*, 2016b]. In addition, an extra compression of the Martian boundaries is expected due to the arrival of a space weather event [e.g., *Opgenoorth et al.*, 2013] as will be analyzed later. Therefore, MEX could have had some small excursions into the solar wind region during this period, and likely, solar wind moments could be extracted. However, currently, there is no automatic way for purely extracting solar wind moments in a MEX orbit situation such as the one illustrated in Figure 1, as MEX would be insufficiently far from the bow shock. By using the AMDA science analysis system tool [http://amda.cdpp.eu/], the proton (H^+) density, velocity, and dynamic pressure have been estimated and are plotted in Figures 2j–2l, respectively. These factors are derived from the IMA spectrum (Figure 2i). We highlight that these three panels are the result of a mixed source between the solar wind and the magnetosheath regions. Particularly, the H^+ speed is the parameter most affected as the solar wind particles are rapidly decelerated inside the magnetosheath [e.g., *Dubinin et al.*, 2008]. Nevertheless, the time evolution of H^+ density, velocity, and dynamic pressure measured by MEX gives us an indication of how these parameters varied. As shown in Figure 2j, a huge and abrupt density increase took place on 7 March 2008. The H^+ velocity (Figure 2k) also increased from about 250 km/s to 500 km/s in 1 day, similar to the previous observations of STEREO-B at 1 AU. A fast stream then followed where the velocities remained at 400–500 km/s for several days, during which the H^+ density was very low. It should be noted that the shape of the observed variation in velocity and density by STEREO-B and MEX is similar, just delayed by ~1 day, of course after considering all the instrument limitations previously indicated.

Since a parent CME could not be determined for the ICME observed at STEREO-B and possibly observed at Mars, we have performed a WSA-ENLIL + Cone simulation using parameters for a hypothetical CME

erupting on 2 March 2008 at 00:00 UT with a speed of 450 km/s, direction of −38° longitude, −7° latitude and full angular width of 30°. We have plotted the results of the WSA-ENLIL + Cone simulation in Figures 2 (cyan lines) and 3. Although the model gives higher velocity values at both STEREO-B and Mars, in general, the model captures pretty well the increase in velocity. Regarding the H^+ density, the model underestimates the magnitude of the event at both locations, and it predicts that the increase in density arrives a few hours earlier at Mars. This model underestimation is a known limitation of the model, as recently *Dewey et al*. [2016] assessed after comparisons of the WSA-ENLIL + Cone model with observations by the Mars Atmosphere and Volatile Evolution (MAVEN) spacecraft. However, the model at Mars is good in identifying the main event on 7 March and a secondary small density increase on 9 March, consistent with the MEX data measurements. Nonetheless, the modeled disturbance appears to be few hours early when compared to data, both at STEREO-B and Mars. This double event at Mars is evident in the simulation of the interplanetary magnetic field (IMF, Figure 2m), although there is no possibility of a direct comparison with data, as MEX does not have a proper magnetometer.

The event was also seen in data from the Mars Odyssey spacecraft. When a galactic cosmic ray proton enters the atmosphere, it interacts with the neutral atmosphere and produces a nuclear-electromagnetic cascade of secondary particles, such as neutrons [e.g., *Thomas et al*., 2015]. The reflection at the surface of some of the neutrons with high enough energy can be measured in orbit by HEND. Thus, neutron count rates serve as an indirect proxy for GCR flux. Figure 2n shows the percentage of variation in the GCR measured by HEND in Mars's orbit with respect to the maximum level during this period (100%). Small variations in the profile respond to changes in the Martian surface composition sampled by HEND, as different surface strata can produce different levels of neutron absorption. On 8 March 2008, there is a sudden decrease in the amount of GCR flux (for ~12 h), followed by a slow recovery phase that lasts ~12 days (until 20 March). The decrease is small (only 3%) but significant and occurred at the same time that MEX was recording the passage of the space weather event. This kind of reduction is commonly called a Forbush decrease [e.g., *Forbush*, 1938], which is a sudden reduction in the GCR that reaches the planet. It is a consequence of the passage of an ICME, as the shock, sheath, and enhanced magnetic field inside the magnetic cloud of the ICME scatters particles away thereby reducing the observed GCR intensity [e.g., *Cane*, 2000; *Hassler et al*., 2014; *Guo*, 2015]. Therefore, this data can be also considered as a kind of proxy for IMF strength. We note that the unambiguous decrease does not start at exactly the same time that MEX observes the first arrival (it starts few hours after), although there is a small reduction at that point (where red line indicates). This small initial reduction could be associated with a hypothetical shock before the main body of the ICME-like event [e.g., *Richardson and Cane*, 2011], but because the first reduction is not statistically significant, we cannot conclude if this is indeed the shock. It is difficult to determine from these observations when the ICME-like structure arrived in relation to the SIR, as the intrinsic HEND data variability is masking the current arrival time of the ICME-like transient or possibly different positions of MEX and Mars Odyssey around Mars cause this uncertainty.

All the available evidence seems to indicate that there is a high probability that an ICME-like structure indeed arrived at Mars together with the SIR and that the behavior of these two solar wind events and the consecutive fast stream was very similar at both STEREO-B and Mars.

4. Mars Express Observations

The response of the Martian plasma system to such events is analyzed in this section, starting from the most energetic plasma, i.e., altitudes of magnetosheath and upper ionosphere, and moving to the lower energetic plasma, i.e., photochemical ionosphere (maximum ionization region at ~135 km).

4.1. Hot Plasma Population at Spacecraft Altitude

In this section we focus on the suprathermal plasma population (0.001–20 keV) at the spacecraft altitude. We note that hot plasma could also be found at lower altitudes, but Mars Express is not able to measure it. Figure 4 shows 17 ASPERA-3 ELS energy-time spectrograms from across the period of the space weather event. In all panels the electron energy is on the left-hand *y* axis, universal time (UT) is on the *x* axis, and the electron differential energy flux (DEF, units of eV cm^{-2} s^{-1} sr^{-1}) is represented by the colors given in the color bar. The DEF we present in these panels is the average across all ELS anodes not looking across the spacecraft body [see *Frahm et al*., 2006] but includes all ELS data quality flags. White segments of the ELS spectrograms (e.g., 10:45–11:20 UT of orbit 2 and the entirety of orbits 5, 7, and 16) represent no data being available at

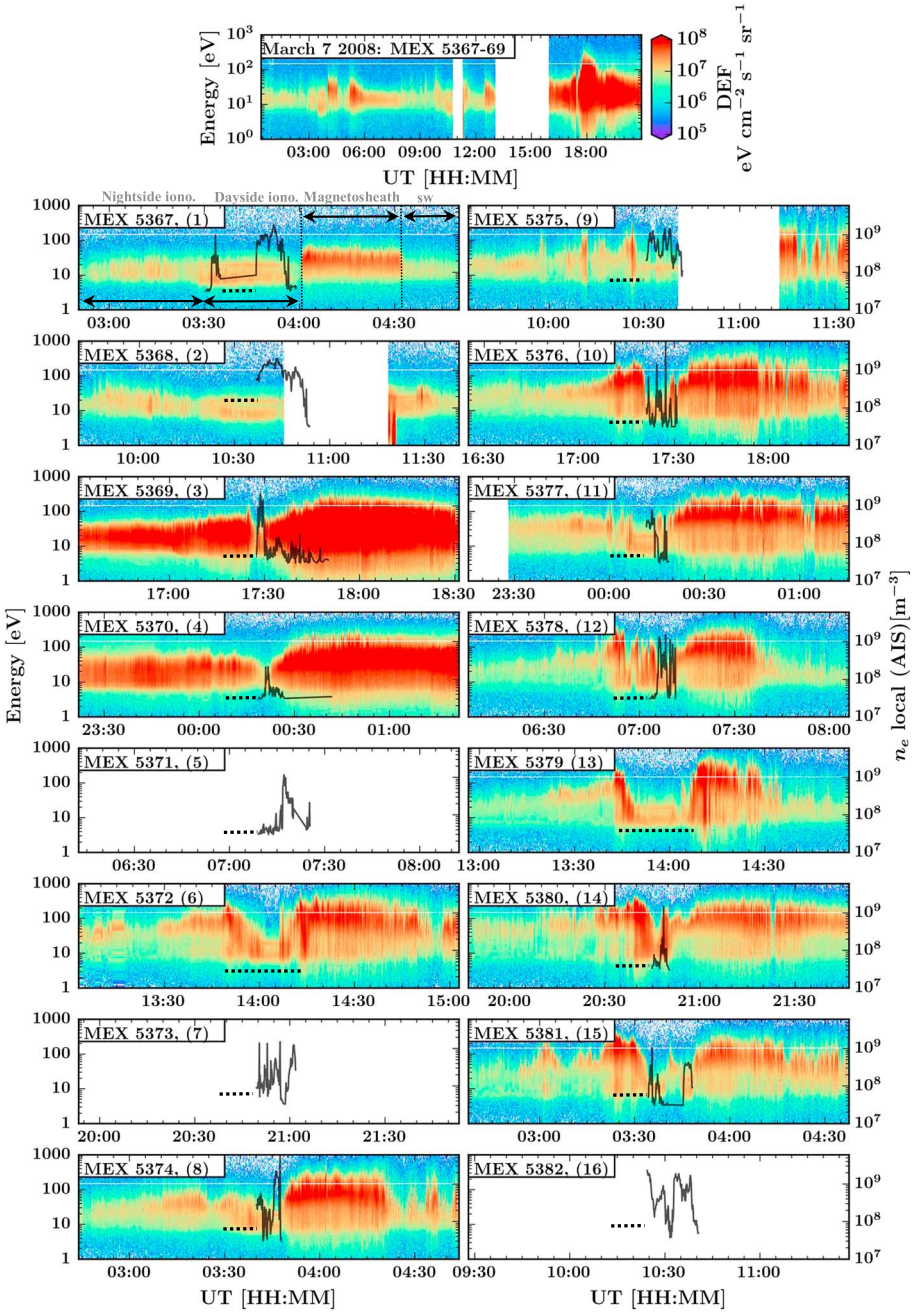

Figure 4. MEX ASPERA-3 ELS energy-time electron differential energy flux (DEF) spectrograms across period of study. (top) ELS spectrum for the entirety of 7 March 2008 (parts of MEX orbits 5367–5369), to indicate the time arrival of the ICME-like structure. (Panels 1–16) Individual orbit spectra centered on MEX periapsis with a duration of ±1 h. In each of these individual orbit spectra, the MARSIS-AIS-derived local electron density is superimposed as a solid black profile, whereas the times in which MARSIS was operated in subsurface mode (lack of local plasma measurements) is represented by a dashed horizontal black line. White blocks represent periods where ASPERA-3 ELS did not accumulate any measurements. Vertical dashed lines in panel of orbit 1 exemplify the boundary identification method used in this work. The different regions transited by MEX are also indicated on the top of the panel of orbit 1. We note that the horizontal white line at 150 eV is an instrumental effect due to the ELS default mode that is broken into two energy ranges, and the separation limit is at that energy level.

all. All panels are labeled with the MEX orbits in which the electrons have been sampled. Orbits 1–16 show the individual orbit spectra centered on MEX periapsis with a duration of ±1 h, where we also superimpose the MEX MARSIS-AIS-derived local electron density (solid black profile) with the scale given on the right-hand *y* axis of these panels. A dashed horizontal black line represents when MARSIS was operating in subsurface mode and thus unable to determine the local electron density. In all of the spectra, a rapid enhancement in DEF across a wide range of energies (up to a few hundred eV) is interpreted as a crossing of MEX into the Martian magnetosheath (e.g., orbit 1 04:00–04:30 UT). This boundary determination follows exactly the same criteria as *Hall et al*. [2016b]. As shown in Figure 1, we expect such crossings into the magnetosheath to be primarily from the Martian ionosphere into the magnetosheath, e.g., orbit 1 at 04:00 UT in Figure 4 (or in reverse for a reduction), although if the bow shock were to be at a lower position, a crossing from solar wind into the magnetosheath (through the bow shock) would manifest in a similar way (e.g., orbit 1 at 04:30 UT). An example of boundary identification is shown in orbit 1 of Figure 4 and, as commented later, in Figure 9.

In order to identify the time of arrival of the ICME-like structure, the top panel shows the ELS spectrogram for the entirety of 7 March 2008 (MEX orbits 5367–5369). In Figure 4 (top), we observe a large enhancement in electron DEF after the data gap (between orbits 5368 and 5369, time in range of 13:00–16:00 UT). This shows that the arrival of the space weather phenomena was at some point after 13:00 UT on March 7. Comparing each of the separate orbit spectrograms (panels in two columns), we see that the enhanced DEF in orbit 5369 (orbit 3) lasts for at least another MEX orbit, with the entirety of the spectra in orbit 5370 (orbit 4) also showing enhanced DEF. Compared with the electron spectra prior to the arrival of the space weather phenomena (orbits 1 and 2), in orbit 3 the duration in which high local electron densities are observed ($>10^8$ m^{-3}) is much shorter, and in orbit 4 its magnitude is dramatically lower. This represents the compression of the Martian-induced magnetosphere and ionosphere and a motion of the inner edge of the magnetosheath region toward Mars. Unfortunately, there is another ASPERA-3 data gap across the next orbit (orbit 5), but the local electron density has started to recover with higher magnitudes over a longer time period once again being observed. By orbit 5372 (6), the electron spectrum has somewhat recovered when compared to orbits 3 and 4, but it is still not quite like the spectra prior to the space weather phenomena (orbits 1 and 2). Orbit 5374 (8) is much more similar to the prespace weather phenomena spectra. We interpret that the behavior of these two orbits (6 and 8) is a consequence of the recovery after the ICME-like impact and of the high solar wind velocity of the fast stream. However, orbits 5375 to 5378 (9–13), which are only under the influence of the fast stream, show a different behavior. There are several short-lasting enhancements in DEF reminiscent of crossings into the magnetosheath from the ionosphere, suggesting high variability in the location of the inner Martian plasma boundary (see Figure 9 for a zoom in this area). Additionally, high electron densities are observed over shorter intervals, which are in opposition with the DEF enhancements, supporting the interpretation of multiple magnetosheath crossings (see Figure 9). Moreover, multiple crossings from magnetosheath to solar wind and vice versa are also observed in the later times of these spectrograms (e.g., orbit 9 at ~11:20–11:30). We interpret that this is the result of a lower position of the outer boundary (bow shock), which coincides with the MEX traveling along the edge of the bow shock position. A more detailed analysis of these movements will be done in the next section. Recovery from this spectrum appears to occur in orbit 5379 (13), with spectra comparable to that in orbit 6, just after the first space weather phenomena arrival. The final orbits in this figure (14–16) once again become disturbed with longer-lasting magnetosheath-like regions, and a local electron density is again observed over shorter intervals. The local electron density profile in orbit 16 looks to have somewhat recovered, although no ELS spectra are available for comparison.

4.2. Cold Plasma Population at Spacecraft Altitude

Regarding the behavior of the thermal population of the ionosphere (main component of the ionosphere), Figure 5 shows 16 MARSIS-AIS spectrograms recorded during the event. The spectrograms are the representation of the carrier MARSIS frequencies in the sounding versus the sampling time. Only frequencies between 0.1 and 2.5 MHz have been plotted since the local plasma density and magnetic field can only be calculated from frequencies in this range. The color code indicates the intensity of the received signal in the sounding [*Morgan et al*., 2013]. In general, greenish to reddish colors are a consequence of ionospheric reflections, and blueish colors indicate their absence. The sharp color change from greenish to blueish at the low frequencies

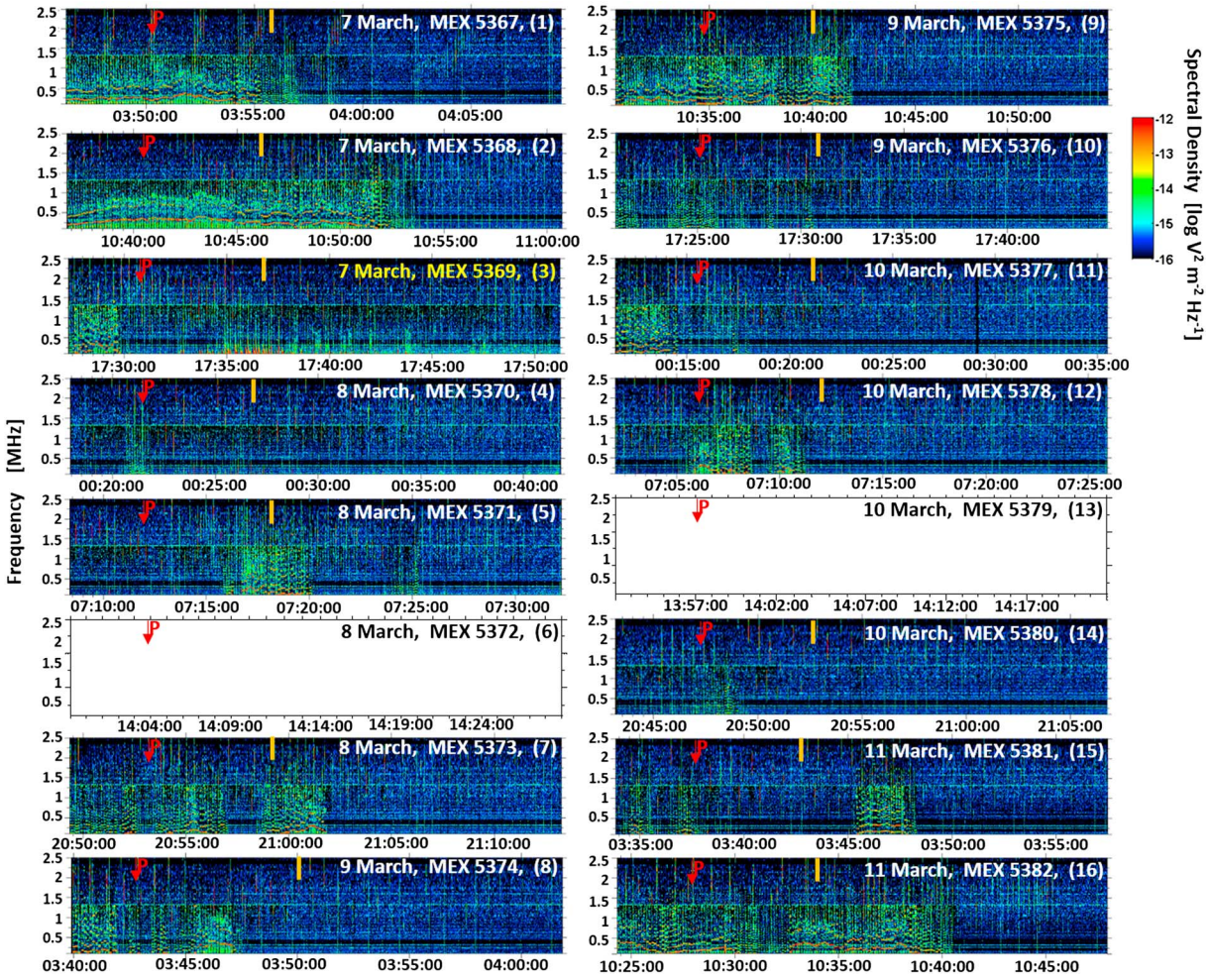

Figure 5. The 16 MARSIS-AIS spectrograms (sounding MARSIS frequencies between 0.1 and 2.5 MHz versus time) from the studied event period. White panels mean no data available for those orbits. The color code indicates the intensity of the received signal in the sounding. In general, greenish to reddish colors are a consequence of ionospheric reflections, and blueish colors indicate their absence (see text for a more detail description). The pericenter of each orbit is marked with a *P*, and a small vertical yellow line in the spectrograms indicates when the spacecraft altitude exceeds 500 km, having a small altitude variation with time before the yellow line (see also Figure 1f).

indicates the position of the ionopause, which is an abrupt break in the ionospheric electron density [*Schunk and Nagy*, 2009] where the spacecraft leaves the ionospheric cold regime and enters other warmer plasma regimes where cold plasma is no longer the dominant component [*Withers*, 2009]. The horizontal lines within the spectrograms are the plasma harmonics at the spacecraft altitude from which the local plasma properties can be derived [*Andrews et al*., 2013]. The almost constant horizontal line at 1.3 MHz in all the spectrograms of the figure is the consequence of an instrumental effect of the MARSIS radar operations. The pericenter of each orbit is marked with a *P*, and a small vertical yellow line in the spectrograms indicates when the spacecraft altitude exceeds 500 km, having a small altitude variation with time before the yellow line (see also Figure 1f). The arrival of the ICME-like event and the SIR occurred at some point just before the third orbit, whose label is marked in yellow. The consistency of the MEX trajectory from orbit to orbit allows us to easily identify changes in the MARSIS data in consecutive orbits, as basically the same regions are sampled from one orbit to the next, only changing the longitude. Therefore, temporal changes observed in the data are due to changes in the plasma region and/or a different spatial configuration of the Martian system boundaries and not because of the spacecraft trajectory. The local (to MEX/MARSIS) plasma density (in blue) and magnetic field magnitude (in green), as derived by the *Andrews et al*. [2013, 2015] automatic algorithms, respectively, are plotted in Figure 6. Both figures are complementary, although Figure 5 shows more information not analyzed here, such us radar absorption or

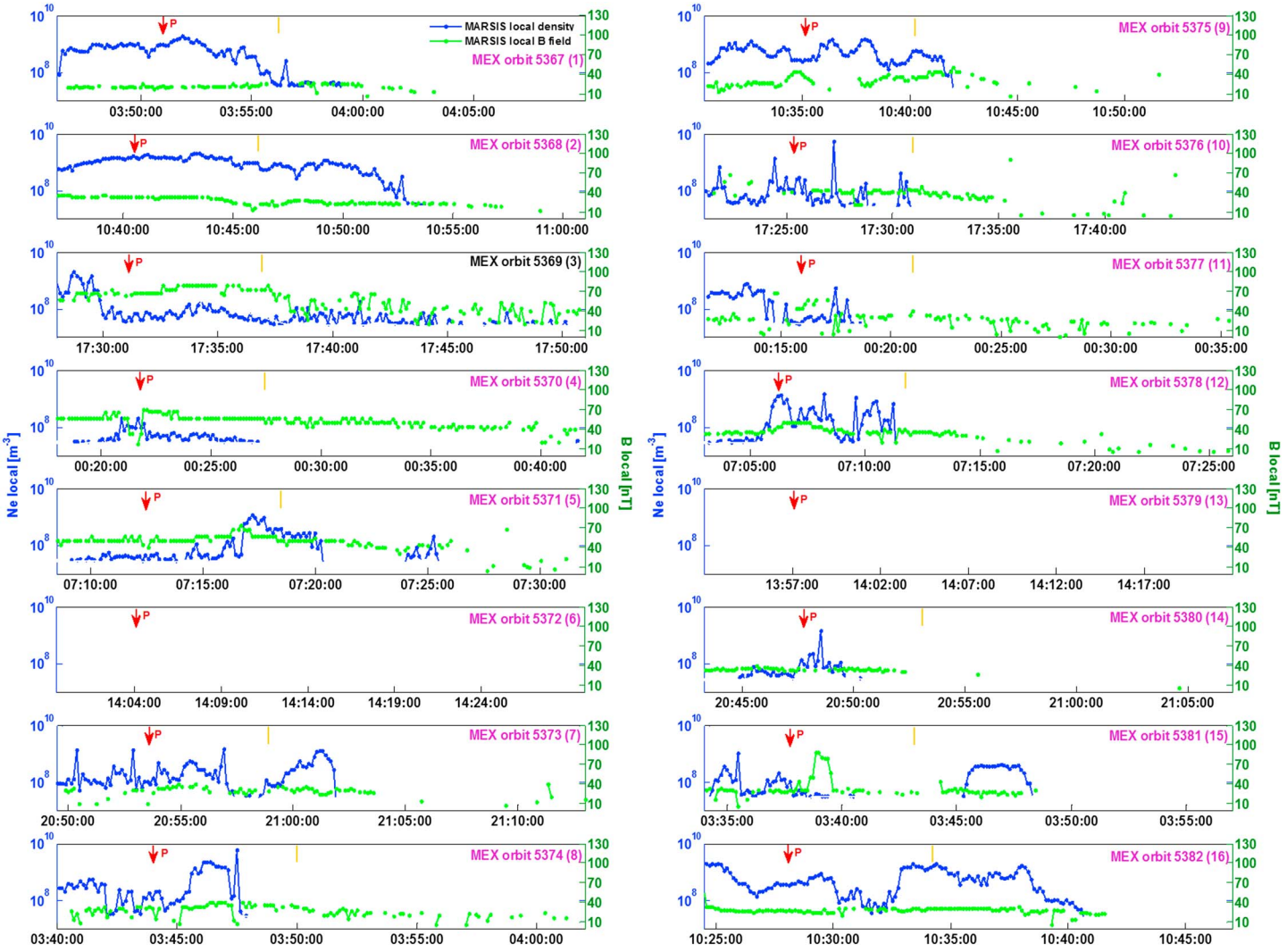

Figure 6. Local plasma density (blue, left *y* axis) and local magnitude of the magnetic field (green, right *y* axis) both at the spacecraft position, derived from MARSIS-AIS data shown in Figure 5 with the *Andrews et al.* [2013, 2015] algorithms. Only data with good flags have been plotted.

changes in signal power intensity. The temporal variation of both figures is the same. Regarding the local density, only data with a good flag after algorithm processing have been considered (more details of this estimation can be found in *Andrews et al.* [2013]). Regarding the local magnetic field, spikes in data have been removed after algorithm processing only when they had a low power signal in the cyclotron traces, when lines were not purely horizontal, and/or those that local plasma was very intense and these echoes were partially hidden. We note that crustal magnetic field at these locations can be neglected since MEX was over the unmagnetized Northern Hemisphere.

In both figures, the two first orbits correspond to measurements before the arrival of the ICME-like and SIR events. A well-extended ionosphere with respect to the spacecraft altitude and MEX passage (as seen by the local plasma) is found at least up to 500 km during the first and second orbits. The local electron density behavior is fairly constant along both orbits, being on average 10^9 m^{-3}. The local magnetic field is ~25 nT for both cases. The values of the induced magnetic field magnitude in this region are similar to those reported by other authors [e.g., *Acuña et al.*, 1998; *Akalin et al.*, 2010; *Modolo et al.*, 2016].

The space weather event arrived at Mars on 7 March during orbit 5369 as seen by ASPERA-3 (Figure 4, top) but before MARSIS started sounding the ionosphere. The third panels in Figures 5 and 6 show the MARSIS-AIS measurements a few hours after the first ICME-like/SIR impacts at Mars. The most evident feature is a

large and nonuniform compression of the ionosphere. We remind the readers that if MEX observes a shorter "ionosphere," i.e., MEX measures the presence of local cold density at the spacecraft altitude $>10^8$ m^{-3} during a shorter interval of time when the orbit trajectory is similar in all the panels, then the ionosphere is more compressed. Alternative interpretations for a short ionosphere as seen by MEX can be the penetration of higher-altitude plasma to lower elevations or erosion of the ionosphere. The former will be analyzed in more detail later, while the latter is difficult to recognize with the current instrumentation. In any case, a plasma population typical of higher altitudes, such as the magnetosheath, is present at the altitude where ionospheric plasma is normally found. The short interval during which MEX detected the ionosphere lasted only for a minute and a half when the spacecraft was at an altitude of ~400 km. During this time, the local plasma density fluctuated between ~10^8 and 10^9 m^{-3} and the local averaged magnetic field was ~70 nT. Surprisingly, a very low local plasma density (below 10^8 m^{-3}) is found at the periapsis, where there is a strong magnetic field signal of 70 nT. The lower density at the periapsis can be interpreted to be an indicator of a nonhomogenous compression due to the solar wind dynamic pressure at the planet. At 17:37 UT, MEX seems to move to another plasma regime, as the frequency of local plasma oscillations changes, and the magnetic field drops to an average 40 nT.

During the fourth orbit, a major compression in the ionosphere is again observed but this time most likely as a result of the pressure of the main body of the ICME-like/SIR. Local plasma densities $>10^8$ m^{-3} are only observed for about 1 min at periapsis altitudes and with extremely weak values, ~10^8 m^{-3}. The local magnetic field remained relatively constant at ~60 nT, with only a small decrease to 40 nT during the small MEX transit to the ionosphere (~00:22 UT).

From the fifth to fifteenth orbits, the behavior of the ionosphere is exceptionally irregular with respect to the normal orbits 1 and 2. This period corresponds to the recovery time of the plasma system after the impact of the space weather event, and also, to when the fast stream was crossing Mars. The mixed structure created by the ICME-like and the SIR events had completely crossed the planet by orbit 7, as the average magnetic field in that orbit diminished to less than 40 nT. However, a large variability in the ionospheric behavior is observed from this orbit that is most likely a result of the solar wind stream, which was characterized by low density and high speed. As commented before, the Martian plasma system was very weak at that time due to the low solar activity phase, which greatly contributes to this large plasma system variability. This is different from the observations of *Opgenoorth et al*. [2013] at the ascending phase of the solar cycle, where the plasma system and the ionospheric thermal pressure were stronger.

During the fast stream, MEX found a very patchy ionosphere with large variations of the local plasma density. There is a compression in the Martian ionosphere, although weaker than after the first impact, with relatively low magnetic field measurements. Orbit 9 shows an apparent "calm" as the behavior resembles that of orbits 1 and 2 before the ICME impact. This could be identified as a full recovery of the system. However, the behavior in the following orbit (orbit 10) clearly differs. As we highlighted in Figure 2, there is a small increase in density and dynamic pressure on 9 March during the high-speed stream that was both observed by MEX with the ASPERA-3 instruments and also predicted by the WSA-ENLIL + Cone simulation. These density and pressure enhancements together with the fast velocity of the solar wind are potentially the reasons for this additional compression of the ionospheric system, where the local plasma density is 10^8 m^{-3} on average, similar to that during the ICME event, with some spikes with values larger than 10^9 m^{-3}. An irregular behavior is observed until orbit 14 similar to the behavior after the ICME-like/SIR impacts but at a more moderate scale. In orbit 14, there is again a large compression of the ionosphere, with very weak local plasma density at the periapsis and with a relatively low magnetic field level.

Finally, the ionosphere seems to return to a normal state in orbit 16, in line with the preimpact orbits 1 and 2. Here the local plasma density is on average 10^9 m^{-3}, with the exception of a depression starting at 10:30 that is not related to our study, but it is most probably to a density depression [e.g., *Duru et al*., 2011] or a superthermal electron flux depression or "electron hole" [*Hall et al*., 2016a]. The magnetic field remains lower than 40 nT, similar to preevent orbits.

4.3. Cold Plasma Population in the Photochemical Region

Figure 7 shows the response of the lower ionosphere in the photochemical region (cold plasma with energies <1 eV, typical altitude ranges ~80–200 km) for the same overall duration as Figures 5 and 6 (i.e., orbits 1–16).

For the part of each orbit highlighted by the salmon box in Figure 1, we plot the estimated induced magnetic field as the difference between the local value obtained from MARSIS-AIS data and the *Cain et al*. [2003] magnetic field model (Figure 7a), the local plasma density at the spacecraft position (Figure 7b), the density and altitude of the main peak of the ionosphere (maximum of ionization region, Figures 7c and 7d, respectively), and TEC of the topside and TEC of the full ionosphere (Figures 7e and 7f, respectively) as blue dots. The salmon box in Figure 1f covers the narrow extent of SZA 38.5–45° and latitude 45–55° and therefore represents similar conditions for each orbit. The average of each value per orbit passage is shown by the red profile, which is discontinued when consecutive orbits do not have data. The difference between the maximum and minimum values of each parameter during each orbit gives an estimate of the variability of the ionosphere in this narrow region. The crustal magnetic field at the spacecraft altitude, based on the Cain model, is expected to be smaller than 10 nT in all the locations of this study. We note that TEC of the full atmosphere (Figure 7f) comes from MARSIS when operating in the subsurface mode, while the rest of the parameters are from the AIS mode. Since MARSIS cannot work simultaneously in both modes, the TEC of the full atmosphere (Figure 7f) comes from the same orbits but a different position over the planet and a larger SZA. Specifically, the TEC from the subsurface mode comes from a region sampled during 10 min before the radar started to work in AIS mode, covering the region from the Martian North Pole to ~62° latitude. To be as consistent as possible with respect to AIS data, we have only plotted the subsurface data closest to the AIS mode data, i.e., SZA between 50 and 60° and latitude between 62 and 75°. Therefore, the TEC magnitude cannot be directly compared with the topside TEC magnitude, as the SZA in both cases is different. Nevertheless, we can consider that the external solar wind conditions are similar when MARSIS was working in each operational mode (only a few minutes of difference), and we can assume that if we observe TEC variations from orbit to orbit, they are caused by the same source. Finally, we note that there is a lack of data in orbit 5 in Figure 7b, while there are data for the same orbit in Figure 6. This is a consequence of the SZA and latitude intervals selected for this comparison (see also the lack of cyan crosses in Figure 1 and the reduced local electron density of Figure 6, both for the salmon region). As a result, Figures 7b–7e do not show any data for orbit 5 because the electron density profiles could not be retrieved due to this very low local electron density, which is a determinant factor [see, e.g., *Sánchez-Cano et al*., 2012].

As mentioned before, the induced magnetic field experienced a large increase after the arrival of the ICME and SIR events (orbit 3, after green arrow in Figure 7a), which lead to a strong compression of the Martian plasma system as seen by the local plasma almost completely disappearing (orbit 4, Figure 7b) at the spacecraft altitude. For the rest of the orbits, the local plasma behaves irregularly, due to the fast stream as previously described in Figure 6. The peak density and corresponding peak altitude of the ionosphere's main layer are shown in Figures 7c and 7d, respectively. For the average conditions of this study, i.e., SZA = 40°, $F_{10.7}$ = 70, and heliocentric distance = 1.644 AU, the main peak is typically located at 130–135 km altitude with a characteristic electron density value of $1.2 \cdot 10^{11}$ m^{-3} [e.g., *Sánchez–Cano et al*., 2013]. As photochemical processes control the behavior of this layer up to 170–200 km of altitude [e.g., *Schunk and Nagy*, 2009], no apparent influence of space weather is observed on the peak density [*Morgan et al*., 2014], which remains on average almost constant for all orbits, with the only exception of a large variability in orbit 7 during the fast stream (see Figure 7c). However, the altitude of the main peak is clearly reduced by ~20 km in orbit 4 at the time that the main body of the ICME-like event crossed the planet. Unfortunately, we do not have data for orbits 5 and 6 in this interval of latitude/SZA to analyze the evolution of the peak altitude, but from orbit 7 to the end, the altitude remains, on average, constant at ~130 km. Figures 7e and 7f show the topside and full ionosphere TEC, respectively. On an orbit by orbit basis, there are some notable differences in the TEC variability. During orbits 2, 3, and 4, the most constant topside variation is found, the ΔTEC ~ $1 \cdot 10^{15}$ m^{-2} per orbit, while during the fast stream (orbits 7–16), the variability is 3 times larger (ΔTEC ~ $3 \cdot 10^{15}$ m^{-2}). The average topside TEC varies little from orbit to orbit, although orbits 4 and 8 have slightly lower values of topside TEC. This is consistent with a reduction of the topside ionosphere due to a more intense-induced magnetic field [e.g., *Ramírez-Nicolás et al*., 2016, and references therein], but the difference is not statistically significant. Regarding the TEC of the full atmosphere, there are no notable variations on average among orbits, which indicate that the density column remained constant during and after the impact of the space weather event. We note, however, a large variability of the full TEC during orbit 3 when the topside TEC was slightly smaller and less variable. A redistribution of the ionization to lower altitudes could have happened, as the magnitude of the full TEC is up to ~$1 \cdot 10^{16}$ m^{-2}, which is a very large value for SZA = 50–60° during the low solar activity

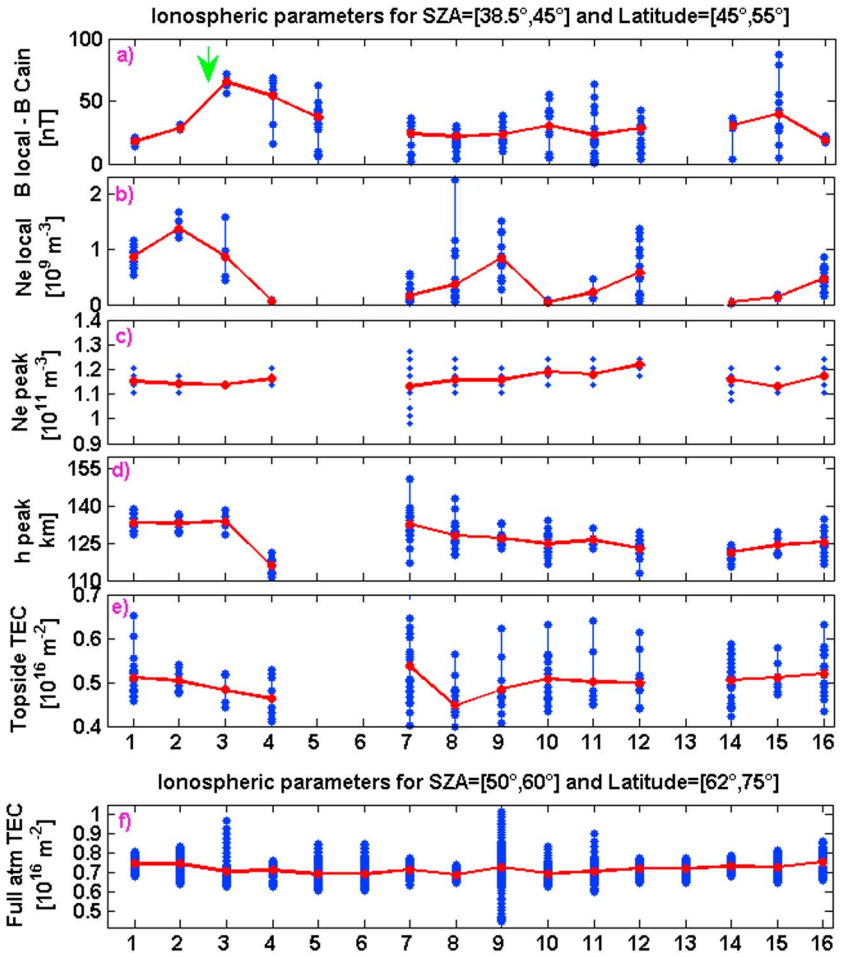

Figure 7. Cold (energies <1 eV) and lower ionosphere during the studied period for the narrow interval of latitude 45–55° and SZA 38.5–45°, which was highlighted in salmon color in Figure 1. Data from every single orbit have been plotted together with blue dots. The average value for each orbit is shown in red. The arrival of the space weather event is marked with a green arrow. Numbers in abscises indicate the orbit number. (a) Local-induced magnetic field (magnetic field estimated at the Mars Express position from MARSIS-AIS data set minus the typical crustal magnetic field at each position as indicated by the *Cain et al.* [2003] model). (b) Local plasma density at the spacecraft position. (c and d) Density and altitude of the main peak of the ionosphere (maximum of ionization region), respectively. (e and f) TEC of the topside from MARSIS-AIS data set and of the full atmosphere from MARSIS-subsurface data set, respectively. We note that TEC in Figure 7f has different latitude (62–75°) and SZA (50–60°) conditions (see text) because MARSIS cannot work simultaneously in both operational modes.

phase, and it is significantly larger than the topside TEC (up to ~$0.5 \cdot 10^{16}$ m^{-2}). Other evidence is that this did not occur for the rest of the orbits. This redistribution means that a possible violation of the hydrostatic equilibrium in the ionosphere, as ions that are normally found in the photochemical region, would be found at lower altitudes. Unfortunately, Mars Express does not have other instrumentation to go deeper in this analysis. Additionally, large variability is observed in orbit 9 during the fast stream that coincides with the higher solar wind density noted in Figure 2 and with also a large variability in the topside TEC. We note that this case is different to orbit 3 because the variability in both the topside and the full atmosphere TEC is similar.

5. IMB Fast Motions

As mentioned before and based on the *Edberg et al.* [2008] model predictions, it was expected that the MEX orbit configuration during the studied period would not allow for the study of the solar wind. However, the reality is that both the inner and outer Martian boundaries were found closer to the planet, mainly due to the

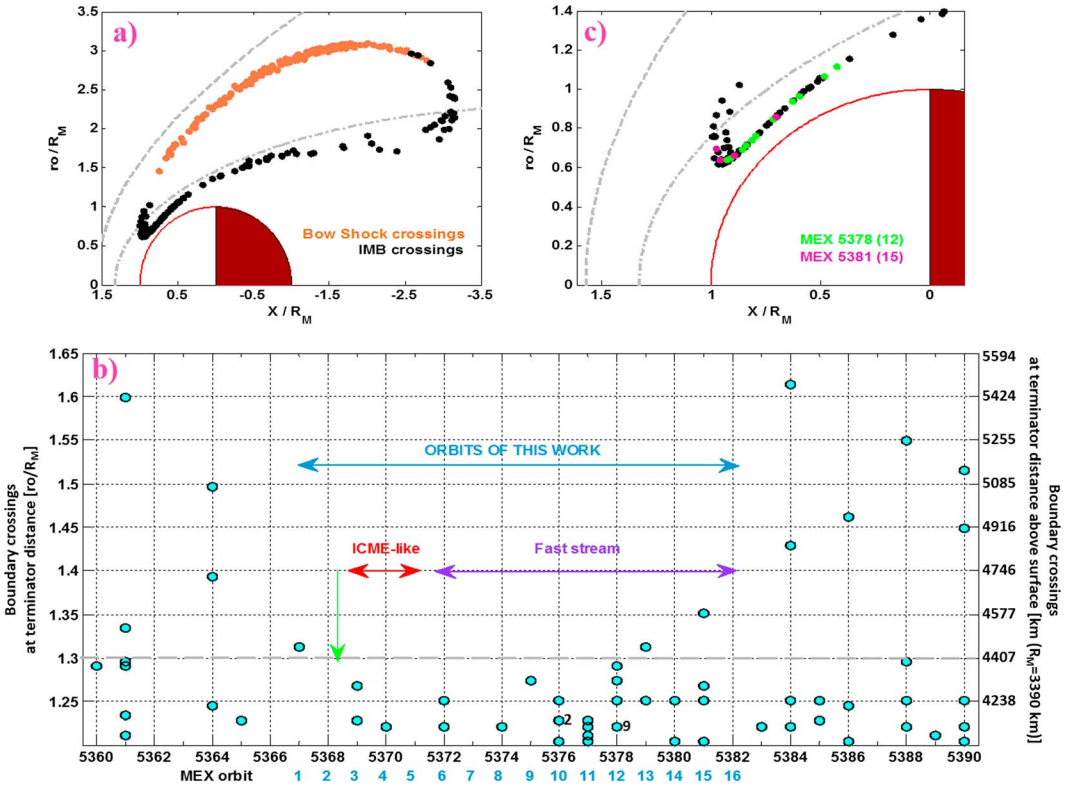

Figure 8. (a) Bow shock (orange) and MPB/IMB (black) crossings detected by MEX between orbits 5360 and 5390. Crossings are plotted in a MSO cylindrical coordinate system and model boundaries come from *Edberg et al.* [2008]. (b) Inner boundary crossings altitude in the dayside extrapolated to the terminator plane and plotted with the MEX orbit number. The number of overlapping crossings has been added next to the corresponding points where there are multiple crossings close to each other. The grey dash line remarks the distance 1.3 R_M (see text). (c) Zoom on the inner boundary crossings on the dayside. There are crossings from two specific orbits highlighted in green and magenta as example orbits of different boundary motions (see text).

combined effects of the low solar activity level, the large heliocentric distance, and the effect of the space weather events analyzed in this work [*Hall et al.*, 2016b]. Indeed, the MEX orbit transited almost the same position of both boundaries, which allows us to assess their shapes and motions. This is especially important close to the subsolar point because this is an area not often transited by MEX. Multiple crossings per orbit are obviously expected since MEX and the boundaries have, on average, similar positions. For simplicity, we call "boundary motion" every time that MEX crosses a region of magnetosheath plasma. Later, we will assess the possibility of being a real motion or just a magnetosheath plasma cloud within the ionosphere.

Figure 8a shows the MEX crossings of both boundaries during this studied period in MSO coordinates, with outer boundary (bow shock) and inner boundary (IMB) as orange and black circles, respectively. We assume that MPB and IMB are practically the same boundary in the dayside regions sampled by this study. For a broader view of the boundary motion, we have added 15 additional consecutive orbits to the ones of this study, making a total of 31 orbits (from 5360 to 5390). These additional orbits have also similar orbital characteristics to the ones described in Figure 1. The crossings were manually identified by using the ELS spectra (Figure 4), following the same criteria described in *Hall et al.* [2016b], plus considering the location of the rapid reduction of the local plasma when MEX left the ionosphere region (e.g., black dotted lines in Figures 4 and 9). The reason for manually identificating the boundaries rather than using an automatic algorithm was due to the difficulties in detecting several multiple crossings occurring within few minutes of duration. As *Hall et al.* [2016b] have recently shown, an automatic algorithm can actually be less sensitive to identifying multiple crossings within the same orbit. We note that the *Hall et al.* [2016b] method is focused in the identification of the bow shock only. Nevertheless, the same method with ELS data can also be

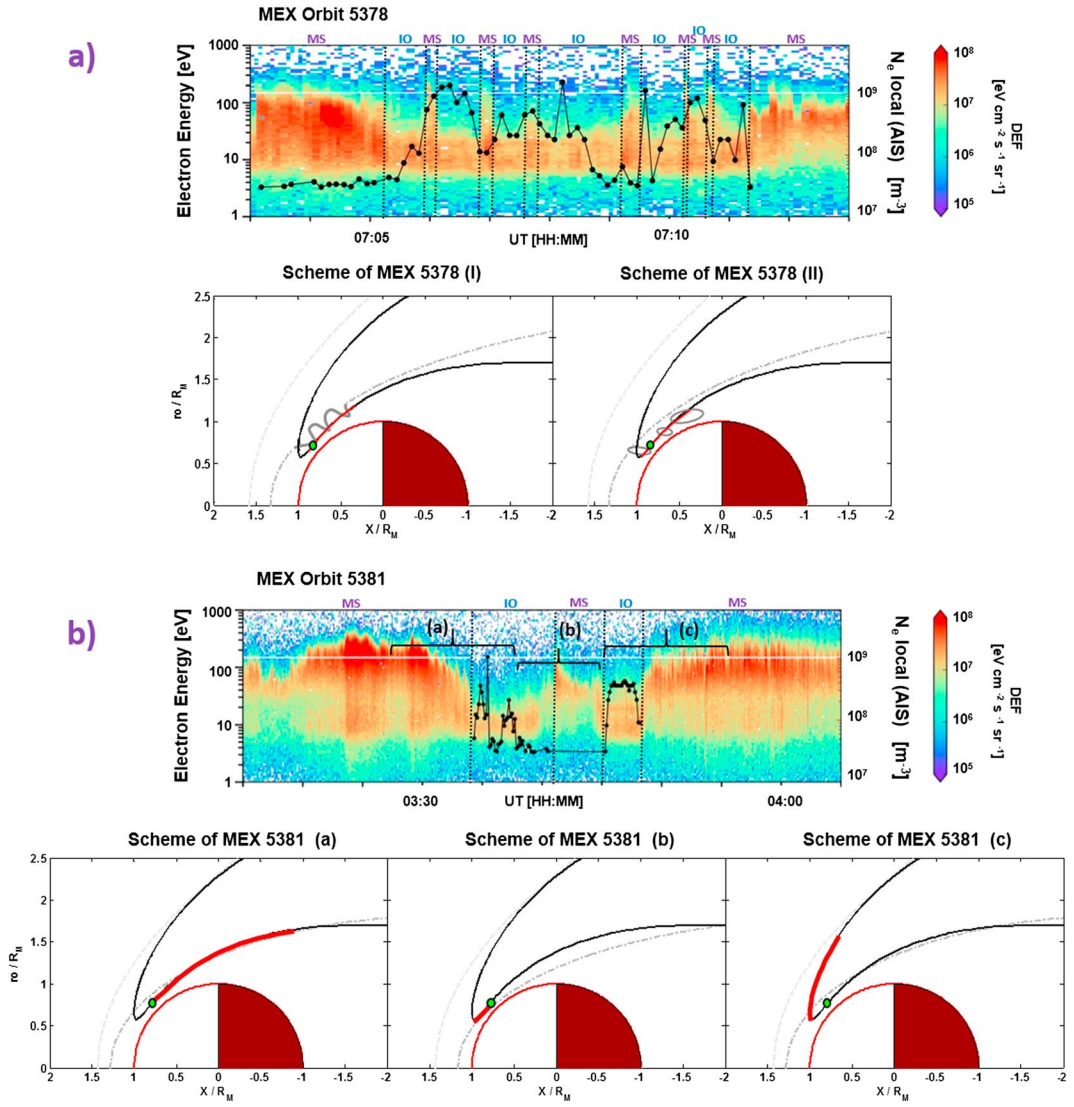

Figure 9. (a) (top) ELS spectrogram (in color-code) and MARSIS local plasma density (in black profile) of orbit 5378 and (a) (bottom) scheme of boundary motion associated to Figure 9a (top) spectrogram as described in the text (not to scale). It shows typical irregularities of the IMB boundary crossed by MEX when traveled parallel to the boundary. (b) (top) ELS spectrogram (in color code) and MARSIS local plasma density (in black profile) of orbit 5381. (b)(bottom) Scheme of boundary motion associated to the top panel spectrogram as described in the text. It shows a three-step radial movement of the boundary when MEX traveled perpendicular to the boundary. Vertical dashed lines indicate the ionosphere-magnetosheath boundary. MS stands for magnetosheath region and IO for ionospheric region. Green dots indicate the pericenter of the orbit.

applied for the IMB in the dayside, because the rapid energy enhancement that delimits the boundary in the dayside is similar to when MEX goes from solar wind to magnetosheath than to when MEX goes from the ionosphere to magnetosheath (in terms of electron energy enhancements). Possible systematic errors due to the manual inspection can be present in the identification. However, we consider that they are of the order of ~80 km maximum (0.024 Mars's radii), as determined from considering the MEX average speed, 4 km/s, the time between two ELS consecutive measurements, 4 s, and that the error in the manual boundary location is not larger than five consecutive ELS measurements. Furthermore, we can consider that our results are robust, as the boundary identification in our study has been done with the same qualitative criteria that *Hall et al.* [2016b] used in their algorithm. Illustrations of the resulting identifications are shown in Figure 4 panel of orbit 1 and in Figure 9, in both cases with vertical black dashed lines.

As the identified bow shock motions in the ELS spectra are most probably the result of MEX skimming along the edge of the boundary, we only focus on the inner boundary motions in the dayside ($+X_{MSO}$, SZA $< 90°$). Also, this region corresponds to the period around MARSIS AIS measurements. To remove the SZA dependence and compare all crossings directly with each other, every inner boundary crossing in the dayside has been projected to the terminator plane by using the *Edberg et al*. [2008, 2009] and *Hall et al*. [2016b] procedure. In short, crossings are rotated by 4° about the MSO *z* axis to consider the perpendicular movement of Mars relative to the solar wind flow direction. Then, a conic section is fitted to each crossing in the cylindrical plane by using the eccentricity and X_0 values from *Edberg et al*. [2008]. The only parameter that varies is the semilatus rectum and allows for obtaining the terminator distance. The results are shown in Figure 8b, where the altitude above the surface of the planet of each inner dayside boundary crossing at the terminator plane is plotted with the MEX orbit number. The objective of this figure is to evaluate the degree of variation observed in the inner boundary for orbits with similar characteristics (e.g., similar SZA) and assess the effect of the space weather events of this paper in its motion. We note that our study is a low limit profile of the existing boundary motion, as we are only evaluating the boundary region crossed by MEX in its trajectory and not the full boundary motion. As observed in Figure 8b, there is a high natural variability observed in the dayside inner boundary altitude in orbits before (5360–5367) and after (5383–5390) the space weather events occurred. This agrees with previous MEX observations [*Duru et al*., 2014]. The variability can reach ~0.4 R_M (~1360 km) in a short period of time (~typically 20 min for nominal orbits). However, when the ICME-like structure arrived (orbits 3 and 4), a strong compression took place resulting in only 1–2 crossings per orbit. This does not mean that there was no motion, but if any boundary displacement or plasma bubble occurred, then it was below the spacecraft altitude. This boundary motion downward is the result of a strong increase in the solar wind dynamic pressure (Figure 2) [e.g., *Edberg et al*., 2009]. Moreover, more crossings per orbit are observed at similar altitudes as soon as the fast stream dominates, similar to the observations made by *Dubinin et al*. [2009], where it was revealed that a SIR is able to produce large blobs of solar wind plasma that penetrate into the magnetosphere and sweep out dense plasma from the ionosphere. *Dubinin et al*. [2009] also stated that consequently, the topside Martian ionosphere becomes very fragmented consisting of intermittent cold/low energy and energized plasmas. However, we remark that, in our study, the same is also observed before and after the SIR and fast stream occurred but with a smaller number of crossings per orbit. For example, focusing only on altitudes below 1.3 R_M to ensure a skimming crossing of the boundary (below grey dash line in Figure 8b), on average, there are 1.75 crossings per orbit before orbit 5369 (pre-ICME-like event), 3.3 crossings per orbit between orbits 5372 and 5382 (fast stream), and 2 crossings per orbit after orbit 5382 (postfast stream event), considering only orbits with ASPERA-3/ELS data at the level 2 of Reduced Data Record (RDR). This indicates that the fast stream seems to enhance the number of irregularities of the IMB-ionosphere border under steady conditions. Moreover, MEX detected crossings at high altitudes ($>$1.35 R_M) before and after the transit of the space weather events that were not detected during the passage of the fast stream, indicating a compression of the IMB caused most probably by the role of the high velocity in the dynamic pressure. As the IMB location is in principle controlled by the solar wind dynamic pressure [e.g., *Dubinin et al*., 2008], a good knowledge of the role that this parameter plays in the motion of the IMB is needed. However, this examination is not possible to carry out in this case, as the H^+ density and velocity shown in Figure 2 were obtained from a mixed source of solar wind and magnetosheath plasma due to the Mars Express orbit configuration. Therefore, the resulting dynamic pressure magnitude is underevaluated, and we prefer to focus only in the description of the observations and avoid speculations on this topic. Regarding high-altitude crossings ($>$ 1.35 R_M), the origin could be different, as we next analyze.

Figure 8c shows a close-up image of the dayside crossings of Figure 8b but in MSO coordinates. Two orbits are highlighted to show two different kinds of detections. These two orbits are considered as exemplars of the data set.

1. When MEX travels along the structure, irregularities in the shape of the boundaries (e.g., solar wind intrusions or instabilities) can be detected, i.e., green crossings (orbit 5378).
2. When MEX travels across the structure (radial to it), the current movement of the boundary can be detected, i.e., magenta crossings (orbit 5381) which are crossings at ~ 0.9 and 1.1 R_M in the *x* axis of Figure 8c.

In the example orbits, both kinds of crossings were detected within a few minutes, giving us a general idea of the large variability of the inner boundary motion in the full dayside. In both cases, the movements are local

with respect to the MEX motion. Top panels of Figures 9a and 9b show the ELS energy-time spectrogram (from Figure 4) of the two orbits highlighted in Figure 8c, focusing on the MEX pericenter region. As in Figure 4, the local plasma density measured by MARSIS-AIS has been superimposed (solid black profiles). Both spectrograms start and finish when MEX is in the magnetosheath region (higher fluxes across a large range of energies), and for most of the central part of the figure, MEX is transiting the upper ionosphere, i.e., the region where the energy level drops to 10–30 eV, and often, a horizontal line at ~23 eV is clearly visible corresponding to the CO_2 photoelectron peak energy [*Fränz et al*., 2007]. Due to negative spacecraft charging, this peak occurs at lower values than expected. In this region, the local density plasma is normally higher than 10^8 m^{-3} and almost null when MEX is in the magnetosheath. However, in both spectrograms when MEX is transiting the upper ionosphere, there are some quick excursions into regions where high energetic electrons (at the levels of the magnetosheath region) are dominant and local plasma generally rapidly disappears. When this occurs, a boundary crossing is computed as mentioned at the beginning of this section and as indicated in the figure with the black vertical dashed lines. Bottom panels of Figures 9a and 9b show some qualitative illustrations of possible explanations for these crossings (not to scale). In the first case (orbit 5378—green dots in Figure 8c), the crossings most probably occurred when MEX traveled skimming along the structure and numerous plasma blobs were crossed as also indicated by *Dubinin et al*. [2009] and *Duru et al*. [2014]. They could also be a result of Kelvin-Helmholtz instabilities in the velocity shear between the magnetosheath and the ionosphere [e.g., *Terada et al*., 2002]. Both possible scenarios are represented in the panel. The origin of these crossings could also be a radial boundary (bouncing) movement, although this is not so probable since there is no identification of this movement when MEX is at higher altitudes in the same orbit.

In the second case (orbit 5381—magenta dots in Figure 8c at ~ 1 R_M), the crossings most probably occurred when MEX traveled across the inner boundary and quick radial movements (~5 min) were observed (e.g., 3:40–3:45 UT). The spectrogram has been marked with three letters that correspond to three different steps of this motion as seen by MEX, as we analyze the following. In step (a), MEX was traveling in the magnetosheath and then crossed to the ionosphere region at ~3:34 UT. Step (b) corresponds to an instant a bit after when MEX was at its pericenter (~3:40 UT) and a sheath-like structure was detected that lasted for ~5 min. Finally, step (c) shows some minutes after when MEX was at higher altitudes and crossed again a robust ionospheric structure for ~3–4 min (starting at ~3:45 UT) before entering again in the magnetosheath at ~3:48 UT. Between steps (a) and (c), the difference in MEX latitude is ~10° and the altitude variation of the inner boundary is ~0.15 R_M (~500 km). As in the previous case, this kind of crossing could be related to plasma solar wind intrusions (plasma blobs) or instabilities, but this is unlikely since there is a large variation in altitude between both crossings (different kind of motion than orbit 5378). Also, MEX was close to the subsolar point, and it spent a considerable amount of time in positions b and c (Figure 9), where a clear and strong magnetosheath and ionosphere were, respectively, observed in the ELS spectrograms and in the MARSIS local plasma. Moreover, Mars Express transited the magnetosheath region during the periapsis of the orbit where normally only the ionosphere is sampled. Boundary oscillations were previously described by *Gurnett et al*. [2010] and assessed by *Duru et al*. [2014] with three MEX examples. These authors concluded that the assumption of a boundary oscillation in a sinusoidal manner could be realistic, since the oscillation periods were 8.65, 6.37, and 8.25 min, comparable to the period of large amplitude fluctuations at Earth's magnetopause.

Furthermore, crustal magnetic fields could be responsible for such detections because the crossings at higher altitude occurred in the equatorial region of the Southern Hemisphere (Figure 1). It could be an anisotropy between the North and South Hemispheres in the position of the MPB [e.g., *Edberg et al*., 2009]. Further, the IMB location could be affected by the direction of the convection electric field [e.g., *Dubinin et al*., 2012], which can lead to the formation of ionospheric swells and valleys, especially in the regions with crustal magnetic fields. However, we consider that our observations are more likely due to a real inner boundary motion (local) rather than the crustal magnetic fields and/or electric fields; the magnetic field magnitude is expected to be less than 10 nT at 300 km altitude for those MEX crossings [*Cain et al*., 2003].

6. Discussion and Conclusions

We report the observations of two different types of solar wind events that arrived at Mars in a short period and within ~1 day in March 2008 during solar minimum, when the Martian plasma system was at its weakest

during the latest solar cycle. The STEREO-B satellite was ahead of Mars at that time and could be used as a solar wind monitor for Mars.

A small transient interplanetary coronal mass ejection (ICME-like) was detected by STEREO-B satellite on 6 March 2008. Just after the trailing edge of the ICME-like transient, the solar wind increases abruptly to almost 700 km/s which lasted for a few days. This led to the formation of a stream interaction region (SIR) centered on the interface of the fast and the slow solar wind streams. The WSA-ENLIL + Cone model simulation solar wind captured well this increase. Regarding the proton density, the timing is well captured by the simulation, although is less accurate capturing the magnitude variability on the days 6 and 7 at STEREO-B and Mars, respectively.

At Mars, both ICME-like and SIR events arrived practically at the same time on 7 March 2008 as detected by both Mars Express and Mars Odyssey. This study mainly focuses on the Mars Express observations with pericenter within the Northern Hemisphere where the crustal magnetic fields do not play a major role in the ionosphere. A total of 16 MEX orbits, which cover 5 days, have been used in this study. Local plasma (at spacecraft altitude) and electron spectra measurements show a clear compression of the ionospheric system in MEX orbit 5369 due to a higher dynamic pressure level, where the local plasma density is found over shorter intervals of MEX trajectory (suggesting compression) and with the presence of a large-induced magnetic field. The inner boundary is found much closer to the planet than model predicted, as well as the altitude of the main peak of the ionosphere. Measurements of TEC show a possible redistribution of the ionization to lower altitudes in the photochemical ionosphere. The event was followed by a fast solar wind stream, which lasted for several days. The increase in velocity and density was very similar to the one recorded by STEREO-B 1 day before. The following days, a compression in the Martian plasma system, are also observed due to the high speed of the solar wind, although weaker than after the first impact. We observed a natural bouncing of the IMB that was enhanced during the passage of the fast stream, as detected by Mars Express. As some previous work has mentioned, magnetosheath plasma blobs were found in the ionospheric region, and also, large radial movements of the inner boundary of the magnetosheath are clearly observed. However, the fast solar wind stream produces a much larger variability of the boundary motion. Moreover, small increases in density/dynamic pressure within the fast stream play notable roles in the behavior of the plasma at high altitudes (diffusion region, above ~200 km), but not in the photochemical region (below ~200 km), such as compression of the boundaries and ionosphere although not as strong as after the ICME-like/SIR impacts.

We have demonstrated that during the low solar activity period, the reaction of the Martian plasma system to space weather disturbances is highly variable. At moderate and high levels of solar activity, it is well known that a big ICME can produce large increases of energetic electrons, strong compressions of the Martian boundaries and large magnetization of the upper ionosphere. A good example is the double ICME that hit Mars on 8 March 2015 and was studied by the MAVEN mission [*Jakosky et al*., 2015]. This event created a substantial deformation of the bow shock and compression of the entire magnetosphere, large flux ropes (~5000 km altitude) with heavy planetary ions, and an intense magnetic field structure. Also, diffuse auroral emission and strong pickup ion enhancements from the neutral oxygen corona precipitating into the Martian ionosphere were observed. Moreover, the event also compressed the topside of the ionosphere as seen by a rapid increase of O^+ with respect to O_2^+ and CO_2^+ in altitude [*Jakosky et al*., 2015]. On the other hand, we have shown that during low solar activity, after a small ICME structure hits Mars, similar effects, such as large magnetosphere and ionosphere compressions, are found but at a smaller scale than at high solar activity. However, there are some notable discrepancies in the plasma response between solar activity phases. Since Mars does not have a global inner magnetic field, the solar wind interaction is directly dependent on the strength of the ionosphere [*Hall et al*., 2016b]. At solar minimum and in the aphelion of the orbit, we have shown that a small increase in solar wind density or velocity (and so, dynamic pressure in any of both cases) produces large effects in the Martian plasma system as we have shown. However, at moderate solar activity levels, *Opgenoorth et al*. [2013] demonstrated that this is not the case. In their study, they showed that the combination of simultaneously increased velocity and increased solar wind density was a more effective driver for magnetospheric/ionospheric responses than only velocity or density by itself. Therefore, small structures that can be unnoticed at Mars during moderate and high solar activity phases are able to create strong perturbations in the system during low solar activity, which can also affect low ionospheric altitudes. This is evidenced with the passage of the fast stream that produced some magnetosheath-ionosphere

compressions (although smaller than after the ICME-like structure), enhancements on the induced magnetic field, and a notable variability on the TEC of the low ionosphere. Moreover, a large number of IMB crossings were detected by MEX in the dayside, most probably as a result of small dynamic pressure enhancements. However, *Opgenoorth et al*. [2013] demonstrated that the passage of a SIR during moderate solar activity can have a similar effect to those caused by an ICME but with a smaller duration. This was later confirmed at high solar activity by *Jakosky et al*. [2015], where the large ICME of March 2015 was satisfactorily compared to previous statistical studies and SIR events. However, *Jakosky et al*. [2015] did not agree with the results of *Ramstad et al*. [2015], as the latter affirmed that statistically, solar wind density, velocity, and solar EUV play different roles. Specifically, changes in the solar wind velocity play notable effects in modifying plasma dynamics at Mars for both low solar wind densities and EUV intensities in comparison to other periods with high solar wind density and EUV fluxes. *Jakosky et al*. [2015] concluded that different kinds of events induce responses of different magnitude at Mars. We agree that the plasma system behaves differently at high/low solar activity but maybe simply due to the strength of the ionosphere obstacle with respect to the solar wind [*Sánchez-Cano et al*., 2016; *Hall et al*., 2016b]. As in our case study, *Ramstad et al*. [2015] observed that not only dynamic pressure plays a role when density and EUV are very small (like our case study at solar minimum) but also the velocity of the solar wind itself.

There is still a large number of open questions to be answered related to the short-term reaction of the Martian plasma system to space weather activity in the different phases of the solar cycle. Future work will include multispacecraft and simultaneous observations, as well as statistical analysis in order to assess and model the system responses to such short and energetic planetary inputs.

Acknowledgments

B.S.-C., M.L., and S.E.M. acknowledge support through STFC grants ST/N000749/1 and ST/K001000/1. B.E.S. H. acknowledges support from the STFC Ph.D. studentship ST/K502121/1. M.L.M. acknowledges the support of NASA LWS grant NNX15AB80G. P.K.'s work was supported by the PAPIIT grant IA104416. Simulation results have been provided by the Community Coordinated Modeling Center at Goddard Space Flight Center through their public Runs on Request system (https://ccmc.gsfc.nasa.gov/database_SH/Beatriz_Sanchez-Cano_033016_SH_1.php). The WSA model was developed by N. Arge at AFRL, and the ENLIL Model was developed by D. Odstrcil at GMU. STEREO-B data were downloaded from the Operating Missions as a Node on the Internet (OMNIWeb) service. Data analysis of Figure 2 (Mars part) was performed with the AMDA science analysis system provided by the Centre de Données de la Physique des Plasmas (CDPP) supported by CNRS, CNES, Observatoire de Paris, and Université Paul Sabatier, Toulouse. This study was carried out in collaboration with the MUAN network, led by Hermann Opgenoorth. Authors thank the MARSIS and ASPERA-3 PIs for the data availability in the PSA. The three anonymous referees of this work and the Editor are gratefully acknowledged.

References

Acuña, M. H., et al. (1998), Magnetic field and plasma observations at Mars: Initial results of the Mars Global Surveyor mission, *Science*, *279*, 1676–1680.

Acuña, M. H., et al. (1999), Global distribution of crustal magnetization discovered by the Mars Global Surveyor MAG/ER experiment, *Science*, *28*(5415), 790–793, doi:10.1126/science.284.5415.790.

Akalin, F., D. D. Morgan, D. A. Gurnett, D. L. Kirchner, D. A. Brain, R. Modolo, M. H. Acuna, and J. R. Espley (2010), Dayside induced magnetic field in the ionosphere of Mars, *Icarus*, *206*, 104–111, doi:10.1016/j.icarus.2009.03.021.

Alves, M. V., E. Echer, and W. D. Gonzalez (2006), Geoeffectiveness of corotating interaction regions as measured by *Dst* index, *J. Geophys. Res.*, *111*, A07S05, doi:10.1029/2005JA011379.

Andrews, D. J., H. J. Opgenoorth, N. J. T. Edberg, M. Andre, M. Franz, E. Dubinin, F. Duru, D. Morgan, and O. Witasse (2013), Determination of local plasma densities with the MARSIS radar: Asymmetries in the high-altitude Martian ionosphere, *J. Geophys. Res. Space Physics*, *118*, 6228–6242, doi:10.1002/jgra.50593.

Andrews, D. J., N. J. T. Edberg, A. I. Eriksson, D. A. Gurnett, D. Morgan, F. Nemec, and H. J. Opgenoorth (2015), Control of the topside Martian ionosphere by crustal magnetic fields, *J. Geophys. Res. Space Physics*, *120*, 3042–3058, doi:10.1002/2014JA020703.

Arge, C. N., and V. J. Pizzo (2000), Improvement in the prediction of solar wind conditions using near-real time solar magnetic field updates, *J. Geophys. Res.*, *105*, 10,465–10,479, doi:10.1029/1999JA000262.

Arge, C. N., J. G. Luhmann, D. Odstrčil, C. J. Schrijver, and Y. Li (2004), Stream structure and coronal sources of the solar wind during the May 12th, 1997 CME, *J. Atmos. Sol. Terr. Phys.*, *66*, 1295–1309.

Barabash, S, et al. (2004), ASPERA-3: Analyser of Space Plasmas and Energetic Ions for Mars Express, European Space Agency Publication Division, SP-1240, pp. 121–140, Noordwijk, Netherlands.

Boynton, W. V., et al. (2004), The Mars Odyssey gamma-ray spectrometer instrument suite, *Space Sci. Rev.*, *110*, 37–83, doi:10.1007/978-0-306-48600-5_2.

Buonsanto, M. J. (1999), Ionospheric storms—A review, *Space Sci. Rev.*, *88*, 563–601.

Cane, H. V. (2000), Coronal mass ejections and Forbush decreases, *Space Sci. Rev.*, *93*, 55–77.

Cain, J. C., B. B. Ferguson, and D. Mozzoni (2003), An $n = 90$ internal potential function of the Martian crustal magnetic field, *J. Geophys. Res.*, *108*(E2), 5008, doi:10.1029/2000JE001487.

Cartacci, M., E. Amata, A. Cicchetti, R. Noschese, S. Giuppi, B. Langlais, A. Frigeri, R. Orosei, and G. Picardi (2013), Mars ionosphere total electron content analysis from MARSIS subsurface data, *Icarus*, *223*(1), 423–437, doi:10.1016/j.icarus.2012.12.011.

Chicarro, A., P. Martin, and R. Traunter (2004), Mars Express: A European mission to the red planet, European Space Agency Publication Division, SP-1240, pp. 3–16, Noordwijk, Netherlands.

Dewey, R. M., D. N. Baker, M. L. Mays, D. A. Brain, B. M. Jakosky, J. S. Halekas, J. E. P. Connerney, D. Odstrcil, J. G. Luhmann, and C. O. Lee (2016), Continuous solar wind forcing knowledge: Providing continuous conditions at Mars with the WSA-ENLIL + Cone model, *J. Geophys. Res. Space Physics*, *121*, 6207–6222, doi:10.1002/2015JA021941.

Dong, C., et al. (2015), Multifluid MHD study of the solar wind interaction with Mars' upper atmosphere during the 2015 March 8th ICME event, *Geophys. Res. Lett.*, *42*, 9103–9112, doi:10.1002/2015GL065944.

Dubinin, E., et al. (2008), Structure and dynamics of the solar wind/ionosphere interface on Mars: MEXASPERA-3 and MEX-MARSIS observations, *Geophys. Res. Lett.*, *35*, L11103, doi:10.1029/2008GL033730.

Dubinin, E., M. Fraenz, J. Woch, F. Duru, D. Gurnett, R. Modolo, S. Barabash, and R. Lundin (2009), Ionospheric storms on Mars: Impact of the corotating interaction region, *Geophys. Res. Lett.*, *36*, L01105, doi:10.1029/2008GL036559.

Dubinin, E., M. Fraenz, J. Woch, R. Modolo, G. Chanteur, F. Duru, D. A. Gurnett, S. Barabash, and R. Lundin (2012), Upper ionosphere of Mars is not axially symmetrical, *Earth Planets Space*, *64*, 113–120, doi:10.5047/eps.2011.05.022.

Duru, F., D. A. Gurnett, D. D. Morgan, J. D. Winningham, R. A. Frahm, and A. F. Nagy (2011), Nightside ionosphere of Mars studied with local electron densities: A general overview and electron density depressions, *J. Geophys. Res.*, *116*, A10316, doi:10.1029/2011JA016835.

Duru, F., D. A. Gurnett, D. D. Morgan, R. Lundin, I. H. Duru, J. D. Winningham, and R. A. Frahm (2014), Dayside episodic ion outflow from Martian magnetic cusps and/or magnetosheath boundary motion associated with plasma oscillations, *Geophys. Res. Lett.*, *41*, 3344–3350, doi:10.1002/2014GL059954.

Edberg, N. J. T., M. Lester, S. W. H. Cowley, and A. I. Eriksson (2008), Statistical analysis of the location of the Martian magnetic pileup boundary and bow shock and the influence of crustal magnetic fields, *J. Geophys. Res.*, *113*, A08206, doi:10.1029/2008JA013096.

Edberg, N. J. T., D. A. Brain, M. Lester, S. W. H. Cowley, R. Modolo, M. Franz, and S. Barabash (2009), Plasma boundary variability at Mars as observed by Mars Global Surveyor and Mars Express, *Ann. Geophys.*, *27*, 3537–3550, doi:10.5194/angeo-27-3537-2009.

Forbush, S. E. (1938), On world-wide changes in cosmic-ray intensity, *Phys. Rev.*, *54*(12), 975–988.

Frahm, R., et al. (2006), Carbon dioxide photoelectron energy peaks at Mars, *Icarus*, *182*(2), 371–382, doi:10.1016/j.icarus.2006.01.014.

Fränz, M., E. Dubinin, E. Roussos, J. Woch, J. D. Winningham, R. Frahm, A. J. Coates, A. Fedorov, S. Barabash, and R. Lundin (2007), Plasma moments in the environment of Mars, *Space Sci. Rev.*, *126*(1–4), 165–207, doi:10.1007/s11214-006-9115-9.

Futaana, Y., et al. (2008), Mars Express and Venus Express multipoint observations of geoeffective solar flare events in December 2006, *Planet. Space Sci.*, *56*, 873–880, doi:10.1016/j.pss.2007.10.014.

Gosling, J. T., and V. J. Pizzo (1999), Formation and evolution of corotating interaction regions and their three dimensional structure, *Space Sci. Rev.*, *89*, 21–52, doi:10.1023/A:1005291711900.

Grandin, M., A. T. Aikio, A. Kozlovsky, T. Ulich, and T. Raita (2015), Effects of solar wind high-speed streams on the high-latitude ionosphere: Superposed epoch study, *J. Geophys. Res. Space Physics*, *120*, 10,669–10,687, doi:10.1002/2015JA021785.

Guo, J., et al. (2015), Modeling the variations of dose rate measured by rad during the first MSL Martian year: 2012–2014, *Astrophys. J.*, *810*, 24, doi:10.1088/0004-637X/810/1/24.

Gurnett, D. A., et al. (2005), Radar soundings of the ionosphere of Mars, *Science*, *310*, 1999–1933, doi:10.1126/science.1121868.

Gurnett, D. A., et al. (2008), An overview of radar soundings of the Martian ionosphere from the Mars Express spacecraft, *Adv. Space Res.*, *41*, 1335–1346, doi:10.1016/j.asr.2007.01.062.

Gurnett, D. A., D. D. Morgan, F. Duru, F. Akalin, J. D. Winningham, R. A. Frahm, E. Dubinin, and S. Barabash (2010), Large density fluctuations in the Martian ionosphere as observed by the Mars Express radar sounder, *Icarus*, *206*, 83–94, doi:10.1016/j.icarus.2009.02.019.

Hall, B. E. S., M. Lester, J. D. Nichols, B. Sánchez-Cano, D. J. Andrews, H. J. Opgenoorth, and M. Fränz (2016a), A survey of superthermal electron flux depressions, or 'electron holes', within the illuminated Martian induced magnetosphere, *J. Geophys. Res. Space Physics*, *121*, 4835–4857, doi:10.1002/2015JA021866.

Hall, B. E. S., et al. (2016b), Annual variations in the Martian bow shock location as observed by the Mars express mission, *J. Geophys. Res. Space Physics*, *121*, 11,474–11,494, doi:10.1002/2016JA023316.

Hara, T., et al. (2016), MAVEN observations of magnetic flux ropes with a strong field amplitude in the Martian magnetosheath during the ICME passage on 8 March 2015, *Geophys. Res. Lett.*, *43*, 4816–4824, doi:10.1002/2016GL068960.

Harvey, J. W., et al. (1996), The Global Oscillation Network Group (GONG) Project, *Science*, *272*(5266), 1284–1286, doi:10.1126/science.272.5266.1284.

Hassler, D. M., et al. (2014), Mars' surface radiation environment measured with the Mars science laboratory's curiosity rover, *Science*, *343*, 6169, doi:10.1126/science.1244797.

Jakosky, B. M., et al. (2015), MAVEN observations of the response of Mars to an interplanetary coronal mass ejection, *Science*, doi:10.1126/science.aad0210.

Jian, L. K., C. T. Russell, J. G. Luhmann, A. B. Galvin, and K. D. C. Simunac (2013), Solar wind observations at STEREO: 2007–2011, AIP Conf. Proc., 1539, 191, doi:10.1063/1.4811020.

Kaiser, M. L., T. A. Kucera, J. M. Davila, O. C. S. Cyr, M. Guhathakurta, and E. Christian (2008), The STEREO mission: An introduction, *Space Sci. Rev.*, *136*, 5–16, doi:10.1007/s11214-007-9277-0.

Kilpua, E. K. J., et al. (2009), Small solarwind transients and their connection to the large-scale coronal structure, *Sol. Phys.*, *256*, 327–344, doi:10.1007/s11207-009-9366-1.

Kilpua, E. K. J., L. K. Jian, Y. Li, J. G. Luhmann, and C. T. Russell (2012), Observations of ICMEs and ICME-like solarwind structures from 2007 – 2010 using near-Earth and STEREO observations, *Sol. Phys.*, *281*, 391–409, doi:10.1007/s11207-012-9957-0.

Lillis, R. J., D. A. Brain, G. T. Delory, D. L. Mitchell, J. G. Luhmann, and R. P. Lin (2012), Evidence for superthermal secondary electrons produced by SEP ionization in the Martian atmosphere, *J. Geophys. Res.*, *117*, E03004, doi:10.1029/2011JE003932.

Ma, Y. J., X. Fang, A. F. Nagy, C. T. Russell, and G. Toth (2014), Martian ionospheric responses to dynamic pressure enhancements in the solar wind, *J. Geophys. Res. Space Physics*, *119*, 1272–1286, doi:10.1002/2013JA019402.

Modolo, R., et al. (2016), Mars-solar wind interaction: LatHyS, an improved parallel 3-D multispecies hybrid model, *J. Geophys. Res. Space Physics*, *121*, 6378–6399, doi:10.1002/2015JA022324.

Morgan, D. D., O. Witasse, E. Nielsen, D. A. Gurnett, F. Duru, and D. L. Kirchner (2013), The processing of electron density profiles from the Mars Express MARSIS topside sounder, *Radio Sci.*, *48*, 197–207, doi:10.1002/rds.20023.

Morgan, D. D., et al. (2014), Effects of a strong ICME on the Martian ionosphere as detected by Mars Express and Mars Odyssey, *J. Geophys. Res. Space Physics*, *119*, 5891–5908, doi:10.1002/2013JA019522.

Mouginot, J., W. Kofman, A. Safaeinili, and A. Herique (2008), Correction of the ionospheric distortion on the MARSIS surface sounding echoes, *Planet. Space Sci.*, *56*, 917–926, doi:10.1016/j.pss.2008.01.010.

Odstrcil, D. (2003), Modeling 3-D solar wind structure, *Adv. Space Res.*, *32*, 497–506, doi:10.1016/S0273-1177(03)00332-6.

Odstrcil, D., and V. J. Pizzo (1999a), Three-dimensional propagation of CMEs in a structured solar wind flow: 1. CME launched within the streamer belt, *J. Geophys. Res.*, *104*, 483–492, doi:10.1029/1998JA900019.

Odstrcil, D., and V. J. Pizzo (1999b), Three-dimensional propagation of coronal mass ejections in a structured solar wind flow 2. CME launched adjacent to the streamer belt, *J. Geophys. Res.*, *104*, 493–504, doi:10.1029/1998JA900038.

Odstrcil, D., Z. Smith, and M. Dryer (1996), Distortion of the heliospheric plasma sheet by interplanetary shocks, *Geophys. Res. Lett.*, *23*, 2521–2524, doi:10.1029/96GL00159.

Odstrcil, D., P. Riley, and X. P. Zhao (2004), Numerical simulation of the 12 May 1997 interplanetary CME event, *J. Geophys. Res.*, *109*, A02116, doi:10.1029/2003JA010135.

Opgenoorth, H. J., O. Witasse, and P. Withers (2010), Mars upper atmosphere network, American astronomical society, DPS meeting 42, id.30.10, *Bull. Am. Astron. Soc.*, *42*, 1029.

Opgenoorth, H. J., D. J. Andrews, M. Franz, M. Lester, N. J. T. Edberg, D. Morgan, F. Duru, O. Witasse, and A. O. Williams (2013), Mars ionospheric response to solar wind variability, *J. Geophys. Res. Space Physics*, *118*, 6558–6587, doi:10.1002/jgra.50537.

Orosei, R., et al. (2014), Mars advanced radar for subsurface and Ionospheric sounding (MARSIS) after nine years of operation: A summary, *Planet. Space Sci.*, doi:10.1016/j.pss.2014.07.010i.

Picardi, G., et al. (2004), Mars express: A European mission to the red planet, MARSIS: Mars advanced radar for subsurface and ionosphere sounding, European Space Agency Publication Division. SP-1240, pp.51–70, Noordwijk, Neth.

Prise, A. J., L. K. Harra, S. A. Matthews, C. S. Arridge, and N. Achilleos (2015), Analysis of a coronal mass ejection and corotating interaction region as they travel from the Sun passing Venus, Earth, Mars, and Saturn, *J. Geophys. Res. Space Physics*, *120*, 1566–1588, doi:10.1002/2014JA020256.

Prolss, G. W. (1995), Ionospheric F-region storms, in *Handbook of Atmospheric Electrodynamics*, vol. 2, edited by H. Volland, pp. 195–248, CRC Press, Boca Raton, Fla.

Ramstad, R., S. Barabash, Y. Futaana, H. Nilsson, X.-D. Wang, and M. Holmström (2015), The Martian atmospheric ion escape rate dependence on solar wind and solar EUV conditions: 1. Seven years of Mars Express observations, *J. Geophys. Res. Planets*, *120*, 1298–1309, doi:10.1002/2015JE004816.

Ramírez-Nicolás, M., B. Sánchez-Cano, O. Witasse, P.-L. Blelly, L. Vázquez, and M. Lester (2016), The effect of the induced magnetic field on the electron density vertical profile of the Mars' ionosphere: A Mars Express MARSIS radar data analysis and interpretation, a case study, *Planet. Space Sci.*, doi:10.1016/j.pss.2016.03.017.

Richardson, I. G., and H. V. Cane (2011), Galactic cosmic ray intensity response to interplanetary coronal mass ejections/magnetic clouds in 1995 – 2009, *Sol. Phys.*, *270*, 609–627, doi:10.1007/s11207-011-9774-x.

Richardson, I. G., G. Wibberenz, and H. V. Cane (1996), The relationship between recurring cosmic ray depressions and corotating solar wind streams at ≤1 AU: IMP 8 and Helios 1 and 2 anticoincidence guard rate observations, *J. Geophys. Res.*, *101*, 13,483–13,496, doi:10.1029/96JA00547.

Rouillard, A. P. (2011), Relating white light and in situ observations of coronal mass ejections: A review, *J. Atmos. Sol. Terr. Phys.*, *73*, 1201–1213, doi:10.1016/j.jastp.2010.08.015.

Rouillard, A. P., et al. (2011), The solar origin of small interplanetary transients, *Astrophys. J.*, *734*, 7, doi:10.1088/0004-637X/734/1/7.

Safaeinili, A., W. Kofman, J. Mouginot, Y. Gim, A. Herique, A. B. Ivanov, J. Plaut, and G. Picardi (2007), Estimation of the total electron content of the Martian ionosphere using radar sounder surface echoes, *Geophys. Res. Lett.*, *34*, L23204, doi:10.1029/2007GL032154.

Sánchez-Cano, B., O. Witasse, M. Herraiz, S. M. Radicella, J. Bauer, P.-L. Blelly, and G. Rodríguez-Caderot (2012), Retrieval of ionospheric profiles from the Mars Express MARSIS experiment data and comparison with radio-occultation data, *Geosci. Instrum. Methods Data Syst.*, *1*, 77–84, doi:10.5194/gi-1-77-2012.

Sánchez–Cano, B., S. M. Radicella, M. Herraiz, O. Witasse, and G. Rodríguez–Caderot (2013), NeMars: An empirical model of the Martian dayside ionosphere based on Mars Express MARSIS data, *Icarus*, *225*, 236–247, doi:10.1016/j.icarus.2013.03.021.

Sánchez–Cano, B., et al. (2015a), Total electron content in the Martian atmosphere: A critical assessment of the Mars Express MARSIS datasets, *J. Geophys. Res. Space Physics*, *120*, 2166–2182, doi:10.1002/2014JA020630.

Sánchez-Cano, B., M. Lester, O. Witasse, S. E. Milan, B. E. S. Hall, P.-L. Blelly, S. M. Radicella, and D. D. Morgan (2015b), Evidence of scale height variations in the Martian ionosphere over the solar cycle, *J. Geophys. Res. Space Physics*, *120*, 10,913–10,925, doi:10.1002/2015JA021949.

Sánchez-Cano, B., et al. (2016), Solar cycle variations in the ionosphere of Mars as seen by multiple Mars Express data sets, *J. Geophys. Res. Space Physics*, *121*, 2547–2568, doi:10.1002/2015JA022281.

Schunk, R., and A. F. Nagy (2009), *Ionospheres: Physics, Plasma Physics, and Chemistry*, Cambridge Univ. Press, Cambridge, U. K.

Terada, N., S. Machida, and H. Shinagawa (2002), Global hybrid simulation of the Kelvin–Helmholtz instability at the Venus ionopause, *J. Geophys. Res.*, *107*(A12), 1471, doi:10.1029/2001JA009224.

Thomas, S. R., M. J. Owens, M. Lockwood, L. Barnard, and C. J. Scott (2015), Near-earth cosmic ray decreases associated with remote coronal mass ejections, *Astrophys. J.*, *801*, 5, doi:10.1088/0004-637X/801/1/5.

Vignes, D., C. Mazelle, H. Rme, M. H. Acuna, J. E. P. Connerney, R. P. Lin, D. L. Mitchell, P. Cloutier, D. H. Crider, and N. F. Ness (2000), The solar wind interaction with Mars: Locations and shapes of the bow shock and the magnetic pile-up boundary from the observations of the MAG/ER experiment onboard Mars Global Surveyor, *Geophys. Res. Lett.*, *27*, 49–52, doi:10.1029/1999GL010703.

Withers, P. (2009), A review of observed variability in the dayside ionosphere of Mars, *Adv. Space Res.*, *44*, 277–307, doi:10.1016/j.asr.2009.04.027.

Xie, Y. Q., P. B. Zuo, X. S. Feng, and Y. Zhang (2015), Properties of solar wind dynamic pressure pulses at 1 AU during the deep minimum between solar cycles 23 and 24, *Sol. Phys.*, *290*, 1835–1849, doi:10.1007/s11207-015-0700-5.

Yamauchi, M., et al. (2015), Seasonal variation of Martian pick-up ions: Evidence of breathing exosphere, *Planet. Space Sci.*, *119*, 54–61, doi:10.1016/j.pss.2015.09.013.

Zeitlin, C., et al. (2010), Mars Odyssey measurements of galactic cosmic rays and solar particles in Mars orbit, 2002–2008, *Space Weather*, *8*, S00E06, doi:10.1029/2009SW000563.